Studies on Trivalent Cation Conduction in Solids
(固体中の３価イオン伝導に関する研究)

2001

Shinji Tamura

Department of Applied Chemistry
Faculty of Engineering
Osaka University

Preface

The work of this thesis has been carried out under the guidance of Professor Dr. Gin-ya Adachi at Department of Applied Chemistry, Faculty of Engineering, Osaka University.

The object of this thesis is to investigate trivalent ion conduction in solids and to develop new trivalent cation conductors.

The author wishes that the knowledge obtained in this study provides useful suggestions and informations for further development and establishment of the high valent cationic conductors and that the materials would contribute greatly to practical applications.

Shinji Tamura

Department of Applied Chemistry

Faculty of Engineering

Osaka University

Yamadaoka 2-1, Suita, Osaka 565-0871

Japan

December 2000.

Contents

General Introduction

In solutions or molten salts, ionic conduction is very common and liquid phase can also accompany electron in these states. In contrast, electron or hole is the well known conducting species in solids. However, in some solids, the mobile species is limited to an ionic state, and such solids are called "Solid Electrolytes". Solid electrolytes have an unique characteristic that ions macroscopically migrate with accompanying elecric charge, and some solid electrolytes showing mono- or divalent ion conduction have been already put on the market, e.g. lithium batteries for heart pacemaker [1, 2], sensing devices, etc.

Up to now, many investigations have been undertaken on many kinds of solid electrolytes in which the mobile species are monovalent ion such as Ag^+, Cu^+, H^+, Na^+, Li^+, and F^- or divalent ions such as Mg^{2+} [3-7], Ca^{2+} [8-11], O^{2-}, etc. Especially, Na^+ in ß/ß"–alumina and NASICON (Na–Super Ionic Conductor) [1, 12], Li^+ in LISICON (Li–Super Ionic Conductor) [1, 13] and O^{2-} in Yttria Stabilized Zirconia (YSZ) [1] are well known species, and the ion conducting properties were intensively investigated so far. In general, the ionic mobility in solid electrolytes strongly depends on the valency and ionic size of the conducting ion. The mono- and divalent cationic conductors, therefore, show a high ionic conductivity. In contrast, trivalent cation has been believed to be very poor migrating species in solids due to the strong electrostatic interaction between trivalent cation and the surrounding anions constituting the lattice.

Ln^{3+}-ß"-alumina [14-21], ß-$LaNbO_3$ [22], Ln-$Al_{11}O_{18}$ [23], and $LaAl_{12}O_{18}N$ [23, 24] were claimed for trivalent cationic conductors. However, only probability of the trivalent cation migration was reported for these solid electrolytes and a direct and quantitative investigation has not been carried out at all. In addition, since Ln^{3+}-ß"–alumina was prepared by ionically exchanging the Na^+ site in ß"–alumina for Ln^{3+}, Na^+ ion still remains and Na^+ ion conduction occurs more or less.

For the realization of the trivalent cation conduction, the mobile ion species should be

selected from the consideration of the trivalent ion properties such as stability and the ionic size, that is, relatively small in ionic radius. In addition, the framework of solid electrolytes should possess a larger tunnel size for ion migration owing to reduce the electrostatic interaction between the mobile ions and anions comprising the framework as much as possible. Recently, the tungstates and molybdates with $Sc_2(WO_4)_3$ type structure have been reported as the pure trivalent cationic conductors by Adachi et al [25-37]. The $Sc_2(WO_4)_3$ type structure holds the quasi–layerd structure, which is suitable for ion migration for such high valency cation species as trivalent ions, with including hexavalent tungsten cation, W^{6+}, which bonds strongly to oxide anions by forming WO_4^{2-} tetrahedron unit, resulting in reducing the electrostatic interaction between the mobile trivalent cation and surrounding oxide anions. However, the solid electrolyte with $Sc_2(WO_4)_3$ type structure has a disadvantage that both W^{6+} cation which contributes to realizing the trivalent cation migration in solids might be reduced to lower valence state in a reducing atmosphere and that a high dense sample can not be obtained for these tungstate and molybdate series.

The present work is consisted of two categories. One is to evaluate the trivalent cation conduction in solid from the view point other than the phenomenological electrical behaviors. Another is the development of novel trivalent cation conductors with a high chemical stability and a high mechanical strength. **Chapter 1** deals with the potential energy around Al^{3+} and W^{6+} in $Al_2(WO_4)_3$ single crystal holding $Sc_2(WO_4)_3$ type structure and with the calculation of the electrostatic force between Sc^{3+} and O^{2-} in $Sc_2(WO_4)_3$ solid electrolytes. Furthermore, we calculated the diffusion coefficient of trivalent cation conduction in solids. The calculation of the electronegativity and the degree of covalent bonding of M^{3+} in $M_2(WO_4)_3$ solid electrolytes were also studied by DV–Xα method [38] which is one of the first principle molecular orbital calculations. **In Chapter 2**, the $R_{1/3}Zr_2(PO_4)_3$ (R : rare earths) solid electrolytes with NASICON–type structure were prepared as new trivalent cationic conductors by a sol–gel method, and the trivalent cation conducting properties were investigated. Furthermore, the relationship

between the trivalent cation conductivity and lattice volume of $R_{1/3}Zr_2(PO_4)_3$ was described. **In Chapter 3**, since the $R_{1/3}Zr_2(PO_4)_3$ prepared by a sol–gel method has a low crystallinity, the solid–state reaction with ball milling was applied as a new synthesizing method for the $R_{1/3}Zr_2(PO_4)_3$ preparation in order to improve the low crystallinity of the phosphates and the conducting properties were investigated and compared with the samples obtained by the above mentioned sol–gel method. **Chapter 4** describes the application of the $Sc_{1/3}Zr_2(PO_4)_3$ solid electrolyte for CO_2 sensor and its high sensing performance was demonstrated.

List of Publications

[1] Trivalent Aluminum Ionic Conduction in the Aluminum Tungstate–Scandium Tungstate–Lutetium Tungstate Solid Solution System,

Shinji Tamura, Takashi Egawa, Yusuke Okazaki, Yasuyuki Kobayashi, Nobuhito Imanaka, and Gin–ya Adachi

Chemistry of Materials, **10**, 1958–1962 (1998).

[2] Trivalent Aluminum Ion Conducting Characteristics in $Al_2(WO_4)_3$ Single Crystals

Nobuhito Imanaka, Shinji Tamura, Masamichi Hiraiwa, Gin–ya Adachi, Hanna Dabkowska, Antoni Dabkowski, and John E. Greedan

Chemistry of Materials, **10**, 2542–2545 (1998).

[3] Ceramics Sinterability Enhancement at an Ambient Pressure by the Boron Oxide Addition

Shinji Tamura, Nobuhito Imanaka, and Gin-ya Adachi

Advanced Materials, **11(1)**, 64–66 (1999).

[4] Trivalent Sc^{3+} Ion Conduction in $Sc_{1/3}Zr_2(PO_4)_3$ Solids with NASICON–Type Structure

Shinji Tamura, Nobuhito Imanaka, and Gin–ya Adachi

Advanced Materials, **11(18)**, 1521–1523(1999).

[5] A CO_2 Sensor Based on a Trivalent Ion Conducting $Sc_{1/3}Zr_2(PO_4)_3$ Solid Electrolyte

Shinji Tamura, Nobuhito Imanaka, Masayuki Kamikawa, and Gin–ya Adachi

Advanced Materials, **12(12)**, 898–901 (2000).

[6] Electronic State of the Trivalent Ionic Conductors with $Sc_2(WO_4)_3$ Type Structure

Nobuhito Imanaka, Shinji Tamura, Gin–ya Adachi, and Yoshiyuki Kowada
Solid State Ionics, **130**, 179–182 (2000).

[7] Trivalent Rare Earth Ion Conduction in the Scandium Tungstate Type Structure
Nobuhito Imanaka, Shinji Tamura, Yasuyuki Kobayashi, Yusuke Okazaki, Masamichi Hiraiwa, Tomohiro Ueda, and Gin–ya Adachi
Journal of Alloys and Compounds, **303-304**, 303-306 (2000).

[8] A New Trivalent Cationic Conducting Solid Electrolyte with NASICON Type Structure
Shinji Tamura, Nobuhito Imanaka, and Gin–ya Adachi
Solid State Ionics, **136–137**, 423 (2000).

[9] Single Crystal Growth of Trivalent Ion Conducting Aluminum Tungstate-Scandium Tungstate Solid Solution
Masamichi Hiraiwa, Shinji Tamura, Nobuhito Imanaka, Gin-ya Adachi, Hanna Dabkowska, and Antoni Dabkowski
Solid State Ionics, **136–137**, 427 (2000).

[10] Rare Earth Ion Conduction in Solids
Gin–ya Adachi, Nobuhito Imanaka, and Shinji Tamura
Journal of Alloys and Compounds, in press.

[11] Trivalent Cation Conduction in $R_{1/3}Zr_2(PO_4)_3$ (R : Rare Earths) with the NASICON Type Structure
Shinji Tamura, Nobuhito Imanaka, and Gin–ya Adachi
Journal of Alloys and Compounds, in press.

[12] A CO_2 Sensor Based on a Sc^{3+} Conducting $Sc_{1/3}Zr_2(PO_4)_3$ Solid Electrolyte

Shinji Tamura, Nobuhito Imanaka, Masayuki Kamikawa, and Gin–ya Adachi

Sensors and Actuators, in press.

[13] Trivalent Ion Conducting Behaviors in $(Sc_{1-x}Al_x)_{1/3}Zr_2(PO_4)_3$ Solid Solution

Shinji Tamura, Misato Yamaguchi, Nobuhito Imanaka, and Gin–ya Adachi

in preparation.

[14] Trivalent M^{3+} Cation Conducting Behavior in NASICON Type Structure

Shinji Tamura, Misato Yamaguchi, Nobuhito Imanaka, and Gin–ya Adachi

in preparation

Chapter 1

Trivalent Cation Conduction in Solid Material

1.1. Introduction

In 1995, we successfully demonstrated the trivalent M^{3+} (M=Al, Sc, Er–Lu) conduction in the tungstates with $Sc_2(WO_4)_3$ type structure [25-37] as described in general introduction. In this tungstate series, $Sc_2(WO_4)_3$ shows the highest trivalent cation conductivity and the lowest activation energy [29]. Furthermore, we also succeeded in enhancing the trivalent Sc^{3+} conductivity by forming the $xSc_2(WO_4)_3$–$(1-x)M'_2(WO_4)_3$ solid solutions (M'=Gd [27], Lu [34]) and the $Sc_2(WO_4)_3$–α-Al_2O_3 composites [33, 37]. In addition, we have made clear the trivalent conducting characteristics in the grain by measuring the ion conductivity of the $Al_2(WO_4)_3$ single crystals [39] and $xAl_2(WO_4)_3$–$(1-x)Sc_2(WO_4)_3$ solid solutions [40] which were prepared by modified Czochralski method. These studies provide phenomenological trivalent cation conduction behaviors in solid materials.

In this chapter, we discuss the potential energy in the $Sc_2(WO_4)_3$ type solid electrolyte crystal, the variation of the electrostatic forces during the Sc^{3+} migration in the lattice structure, and the electronic state of the $Sc_2(WO_4)_3$ type structure in order to support the trivalent cationic conduction phenomena by different point of view. Furthermore, we evaluate the diffusion coefficient of the Sc^{3+} ion in the $Sc_2(WO_4)_3$ solid electrolyte.

1.2. Experimental Details

1.2.1. Potential energies around Al and W atoms in the $Al_2(WO_4)_3$ single crystal with $Sc_2(WO_4)_3$ type structure

After the $Al_2(WO_4)_3$ single crystal was made into a sphere shape(diameter : 0.07905 mm), the 6230 reflection data were collected by using four–circle X–ray diffraction (M06XHF22, Mac Science) with Mo–Kα radiation (ϕ=0.5, λ=0.0710.73) at room temperature. The collected data were analyzed according to Willis method [41, 42] which is one of the refinement methods of anharmonic vibration factor of an atom. The details of this analysis are described in the reference [43].

1.2.2. Electrostatic forces deviation during the Sc^{3+} conduction in the lattice

The electrostatic forces appeared between conducting Sc^{3+} and surrounding ions in the conducting ab, bc, or ac planes in $Sc_2(WO_4)_3$ structure were calculated by the following Coulomb's law.

$$F = (1/4\pi\varepsilon_0)q_1q_2/r^2 \qquad (1–1)$$

Here, ε_o, q, and r represent the dielectric constant, charge of ion, and distance between the two ions, respectively. In this calculation, it is assumed that only Sc^{3+} ion moved to the closest Sc^{3+} site in each plane, and the positions of W^{6+} and O^{2-} ions were fixed. Furthermore, only the ions existed within 4 Å distance from the conducting Sc^{3+} ion was taken into accounts.

1.2.3. Discrete-variational Xα molecular orbital (DV-Xα MO) method

The DV-Xα cluster method was used to calculation of the electronic state of trivalent ion conductors. This method is one of the linear combination of atomic orbital (LCAO) MO methods. In this method, the exchange potential, V_{XC}, is described [38] as,

$$V_{xc}(r_\uparrow) = -3\alpha\left[\frac{3}{4\pi}\rho_\uparrow(r)\right]^{\frac{1}{3}} \qquad (1–2)$$

where $\rho_\uparrow$ is the electron density of the cluster used, and α is a constant. In present work, α is fixed to be 0.7, which was found empirically as the most appropriate. In this method, one-electron Hamiltonian matrix elements, H_{ij}, and overlap elements, S_{ij}, are evaluated with the weighted sum of the integral values at the sample points.

$$H_{ij} = \sum_k \omega(r_k)\phi_i^*(r_k)h(r_k)\phi_j(r_k) \tag{1–3}$$

$$S_{ij} = \sum_k \omega(r_k)\phi_i^*(r_k)\phi_j(r_k) \tag{1–4}$$

Here $\omega(r_k)$ represents the reciprocal of the sample point density at r_k. Mulliken population analysis was utilized for the evaluation of the net charge of each atom and the bond overlap populations of each bond to discuss the ionicity and the covalency of bonding state for the migrating trivalent ions.

1.2.4. Diffusion coefficient of Sc^{3+} in $Sc_2(WO_4)_3$

The diffusion coefficient of trivalent Sc^{3+} ion in $Sc_2(WO_4)_3$ solid solution was calculated by the following Nernst–Einstein relation,

$$D = \sigma kT / Nq^2 \tag{1–5}$$

, where D, σ, k, T, N, and q are diffusion coefficient, conductivity, Boltzmann constant, absolute temperature, number of conducting ion in the unit volume, and charge of ion, respectively.

1.3. Results and Discussion

1.3.1. Energy density in the $Al_2(WO_4)_3$ single crystal with $Sc_2(WO_4)_3$ type structure

For the ion migration, ion has to cross over a certain potential wall, which decides the activation energy for the conduction. The potential energy was directly related to the crystal structure and, in particular, to the open space of the conduction pathway. In order to investigate the ion conduction from the view point of potential energy in the crystal, to study the potential on the plane where cation easily migrates is most effective. Figure 1.1 shows the $Al_2(WO_4)_3$ structure. $Al_2(WO_4)_3$ holds a quasi–layered structure and has two–dimensional conducting plane in this structure. The electrical conducting properties to the a-, b-, and c-axis direction were measured for

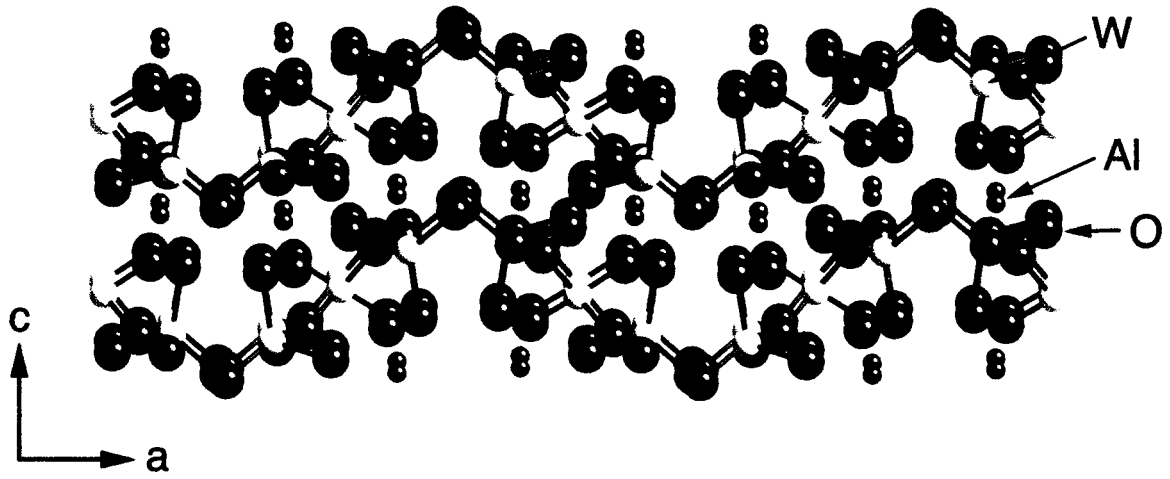

Figure 1.1. Structure of $Al_2(WO_4)_3$ in <010> direction.

the $Al_2(WO_4)_3$ single crystal and are presented in Figure 1.2. Among three axis directions, the conductivity toward the b-axis direction showed the highest value and the conductivity for the a-axis direction was about 1/3 of that for the b-axis direction at 600 °C. In the case for the c-axis direction, the conductivity was two orders of magnitude lower than that for b-axis direction. The pathway where the Al^{3+} ions migrate most smoothly in the $Al_2(WO_4)_3$ grain, is easily speculated to be the b-axis direction, since Al^{3+} ions are not situated in the most suitable site, the center of the

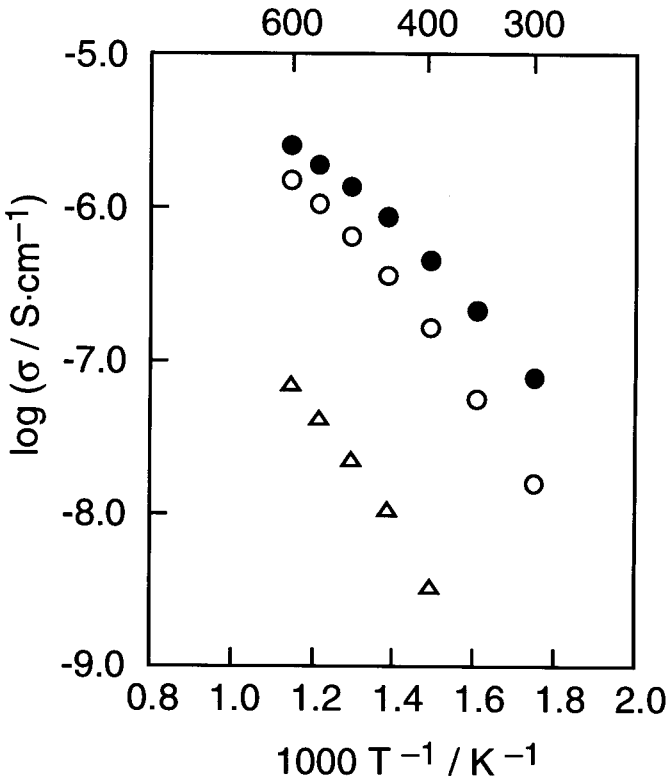

Figure 1.2. Temperature dependencies of the conductivity along each axis for the $Al_2(WO_4)_3$ single crystal (a-axis:○, b-axis:●, c-axis:△).

voids, for the ionic migration to the a-axis direction and for c-axis, the distance between the layers is too narrow for Al^{3+} ion to migrate between them.

As described above, since the conductivities along a-, and b-axis directions in $Al_2(WO_4)_3$ are higher than that of c-axis direction, the potential on ab plane was investigated. Figure 1.3 depicts the potentials around (a) Al and (b) W atoms at room temperature with (c) the corresponding datum of Al atom in Al_2O_3 at 2170K. In this figure, the solid and dashed lines indicate the positive and negative potential, respectively. For the case of W in $Al_2(WO_4)_3$, the tungsten ion was surrounded by high potential wall, and its migration in the crystal is thought to be extremely difficult. On the other hand, the negative potential area exists around Al site (right- and up side in Fig. 3(a)), and

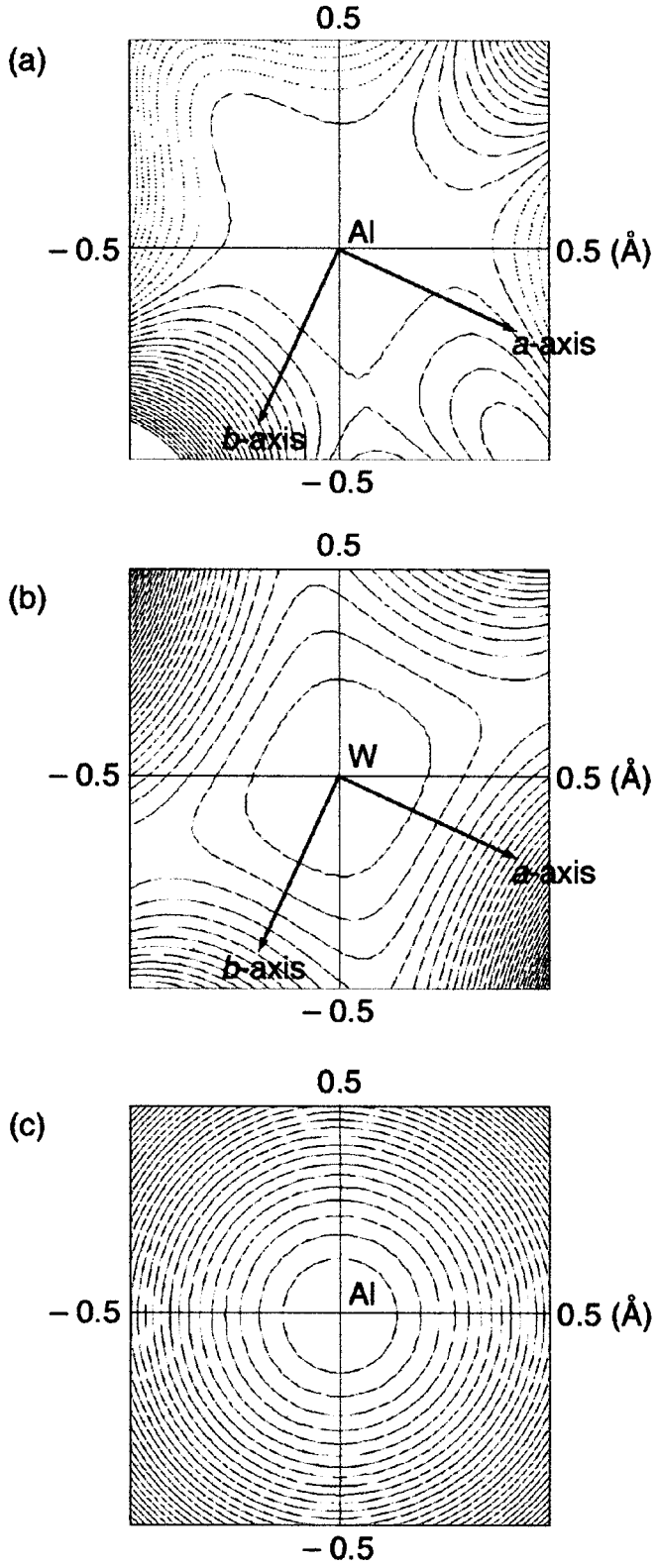

Figure 1.3. The potentials arround (a) Al^{3+} and (b) W^{6+} cations in $Al_2(WO_4)_3$ at room temperature with (c) the potential around Al^{3+} in Al_2O_3 at 2170 K. Contours are at intervals of 2.0×10^{-21} J.

the potential wall in front of the negative area was calculated to be ca. 3.0 x 10^{-21} J. As the translation energy of atom at room temperature is 4.11x 10^{-21} J, the Al^{3+} in the $Al_2(WO_4)_3$ have an enough energy to overcome the potential wall. In the case of Al_2O_3, it is easily speculated that the Al^{3+} ion can not migrate in Al_2O_3 solid because the Al^{3+} ion is surrounded by very high potential walls similar to the case for W^{6+} ion in $Al_2(WO_4)_3$. This result strongly indicates that the high valence cation, W^{6+}, in $Al_2(WO_4)_3$ affects to modify the potential around Al^{3+} ion, resulting in a released circumstance for Al^{3+} ion.

1.3.2. Electrostatic forces between Sc^{3+} and other ions in the $Sc_2(WO_4)_3$ lattice

In order to explain the anisotropic conducting behavior along a-, b-, and c-axis, which are shown in Figure 1.2, the electrostatic force variation was estimated in each conducting plane. Figure 1.4 depicts one of representative model clusters used for this calculation, which is shown a part of the $Al_2(WO_4)_3$ structure. The Sc^{3+}–W^{6+} distance is ca. 3.7Å which is longer than that between Sc^{3+} and nearest O^{2-} ion (ca. 1.8Å). It is well known that the electrostatic force is reduced as increasing the distance between two ions. However, since the W^{6+} has a high valence state, the effect of the electrostatic force should be taken into accounts relatively farther distance. Therefore,

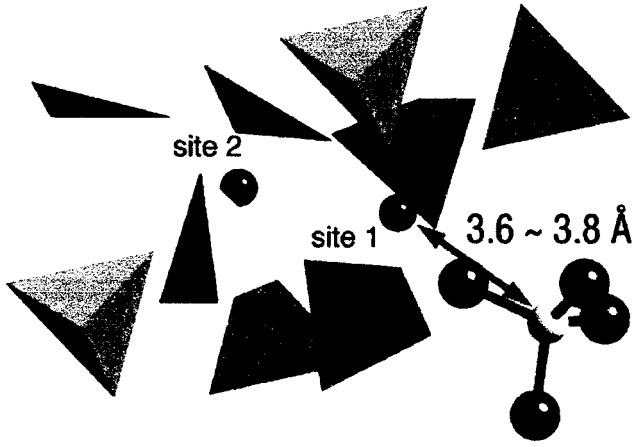

Figure 1.4. A part of the structure utilized for the calculation of the electrostatic force in ab plane.

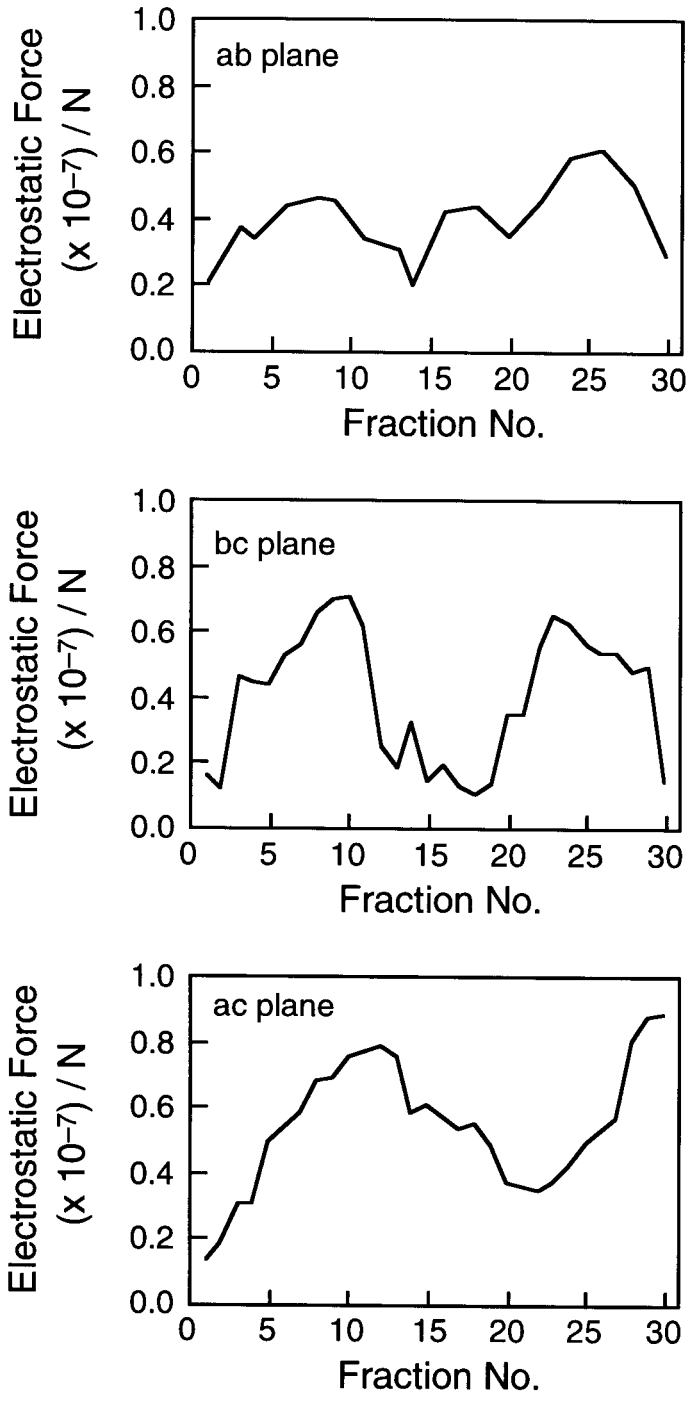

Figure 1.5. The deviation of the electrostatic force between Sc^{3+} and surrounding O^{2-} ions for Sc^{3+} conduction on each plane in $Sc_2(WO_4)_3$ solid.

the calculation was carried out for the Sc^{3+} conducts from site 1 to site 2, and the ions within the distance of 4Å. The calculation results for each plane were shown in Figure 1.5. The maximum force was observed for each case and those maximum values were 6.1 x 10^{-7} N in ab–plane, 7.1 x 10^{-7} N in bc–plane, and 7.7 x 10^{-7} N in ac–plane, respectively. The result suggests that the Sc^{3+} cation easily migrates toward the b-axis which appears in ab- and bc-plane. The c-axis direction is calculated to be most difficult to migrate. Since the order of the electrostatic force is coincided with that of the trivalent cation conductivity in the grain bulk, the anisotropic conducting behavior was found to be predominantly caused by the difference of the electrostatic force during the trivalent cation conduction.

1.3.3. Discrete-variational Xα molecular orbital(DV-Xα MO) method

In order to qualitatively clarify the electronic state of the $Sc_2(WO_4)_3$ type trivalent ion conductors, the DV-Xα MO calculation was carried out with a simple model cluster shown in Figure 1.6. In this model cluster, six WO_4^{2-} units coordinate to a trivalent M^{3+} ion. We have used Al^{3+}, Sc^{3+}, Lu^{3+}, Yb^{3+}, Tm^{3+}, Er^{3+}, and Y^{3+} as the M^{3+} ion and the distance of M-O was estimated from the ionic radius of the trivalent ions in the six–coordinated state and that of oxide ion in the 2 coordinated state. The WO_4^{2-} units were terminated by the point charges in order to neutralize the cluster, since the most important role of ionic interaction with surrounding ions should be charge neutrality of the cluster. This model cluster is the simplest one to discuss the trivalent ion conduction in the $M_2(WO_4)_3$ crystals.

Since the ionic interaction is one of the most important parameters for the ionic conductors, the net charge of the M^{3+} ion is shown in Fig. 1.7(a). The net charge of the M^{3+} ion increases with the increase in the ionic radius of the M^{3+} ions and has a maximum at around 0.10 nm, which is near the radius of the Lu^{3+} and Yb^{3+} ions. As shown in Figs. 1.7(b) and (c), both the net charges of the oxide ions coordinated to the M^{3+} ion and of the W^{6+} ions also become more ionic with increasing

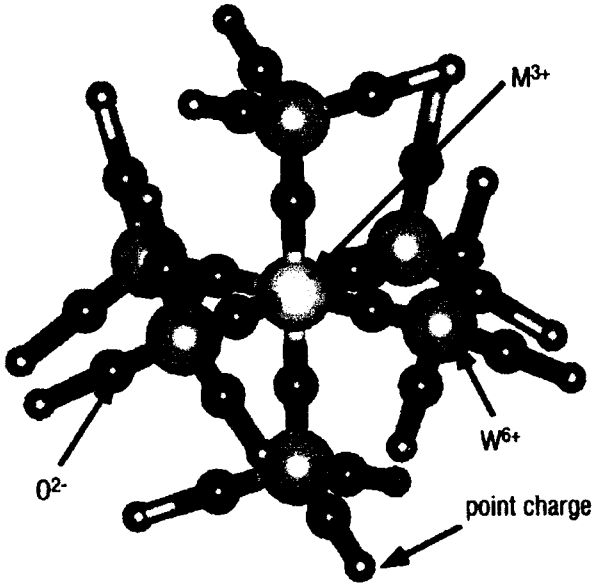

Figure 1.6. The model cluster used for the DV-Xα MO calculation.

ionic radius and the O^{2-} ion has a minimum where as the W^{6+} ion has a maximum at around 0.10 nm.

Though the electronegativity of the M^{3+} ions monotonously decreases with the increase in their ionic radii, the ionicity of the M^{3+} ions has a maximum with the variation of their ionic radii. Since this result might depend upon the covalent interaction between the M^{3+} and the O^{2-} ions, the bond overlap population of the mobile trivalent ion is plotted against the ionic radius in Fig. 1.8(a). The ionic radius dependence of the trivalent ion conductivity is also shown in Fig. 1.8(b) for comparison. The bond overlap population decreases with the increase of the ionic radius and shows a minimum around 0.10 nm. By the further increase of the ion size up to Y^{3+}, the population increases on the contrary. Since the bond overlap population shows the covalency of M-O bond, the smaller covalency of M-O bond could contribute to the smaller activation energy of ionic conductivity of the M^{3+} ion in $M_2(WO_4)_3$ as shown in the Fig. 1.8(b), though their minimums

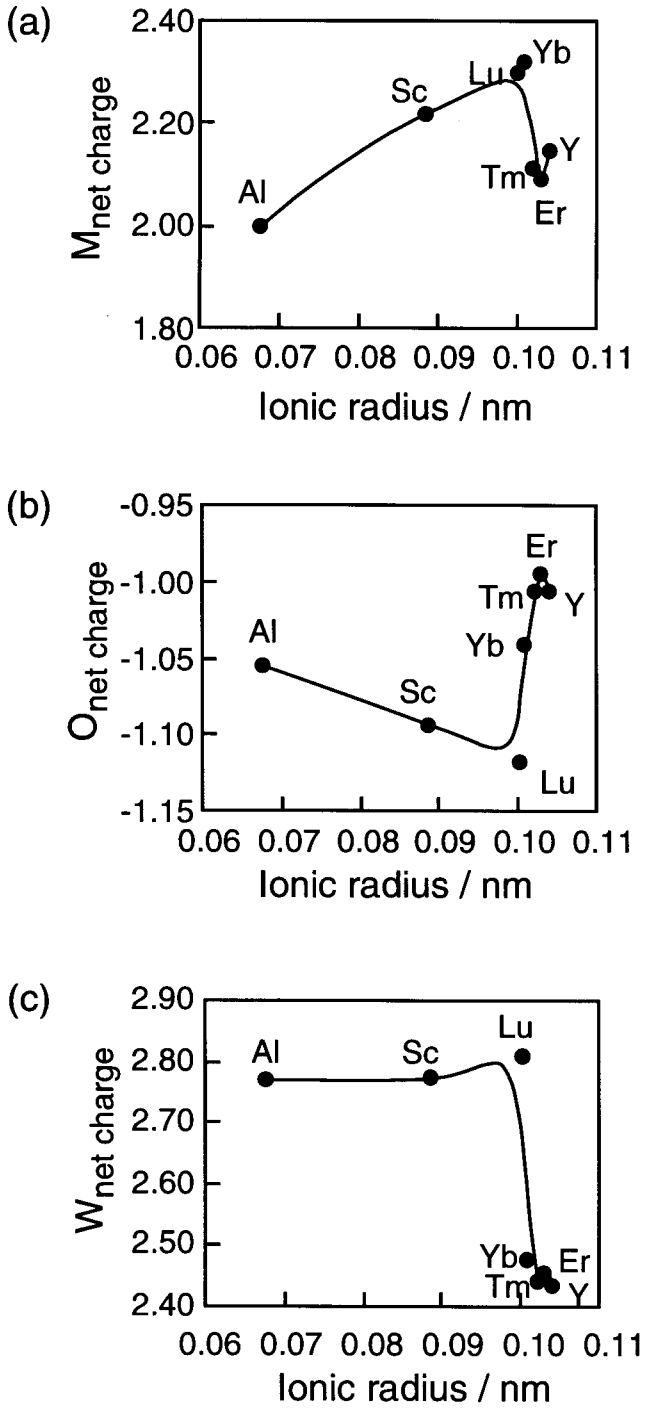

Figure 1.7. The relationship between the ionic radius of the M^{3+} ion and the net charge of (a) the M^{3+} ion, (b) the O^{2-} ion coordinated to the M^{3+} ion, and (c) the W^{6+} ion.

are slightly different from each other. This result suggests that the restraint of the covalent interaction for the trivalent ions should play an important role in the trivalent ion conduction in the $M_2(WO_4)_3$.

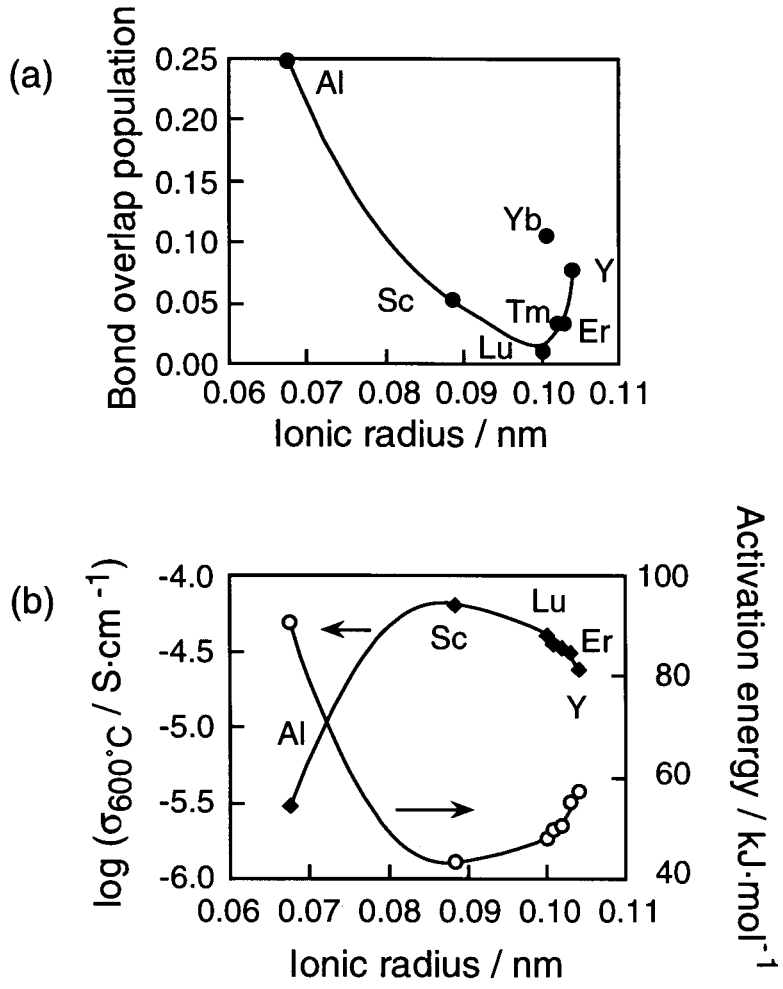

Figure 1.8. (a) The bond overlap population between the M^{3+} ion and the surrounding O^{2-} ions in the $Sc_2(WO_4)_3$ type cluster. (b)The experimentally obtained results of the relationship between the trivalent ion conductivity at 600oC and the trivalent ion radius in the $Sc_2(WO_4)_3$ series for comparison.

1.3.4. Diffusion coefficient of Sc^{3+} in the $Sc_2(WO_4)_3$

Since the concentration of the conducting ion species in solid electrolyte greatly affects the electrical conductivity, the conduction estimated from the conductivity is within the macroscopic migration in solid.

Here, in order to microscopically discuss the trivalent cation migration in solids, a diffusion coefficient was calculated from equation (1-5). Table 1.1 lists the diffusion coefficients calculated for Na^+ in $Na_3Zr_2Si_2PO_{12}$ (NASICON), Mg^{2+} in $Mg_2Zr_2P_6O_{24}$, and Sc^{3+} in $Sc_2(WO_4)_3$. The multivalent cation conduction in solid was easily regarded to be difficult because the diffusion coefficient is greatly lower than that for the monovalent Na^+ cation. Comparing the value of divalent and trivalent, however, the diffusion coefficient of trivalent Sc^{3+} ion in $Sc_2(WO_4)_3$ is only one order of magnitude lower than the divalent. Therefore, it is obvious that the reasonable environment for trivalent cation conduction was realized by selecting the $Sc_2(WO_4)_3$ type structure including hexavalent tungsten ions.

Table 1.1. The diffusion coefficient of various solid electrolytes.

Solid Electrolyte	Conducting Ion Species	Conductivity at 600°C ($S \cdot cm^{-1}$)	Diffusion Coefficient (cm^2 / s)
$Na_3Zr_2Si_2PO_{12}$	Na^+	7.78×10^{-1}	3.33×10^{-9}
$Mg_3Zr_4P_6O_{24}$	Mg^{2+}	1.47×10^{-5}	2.75×10^{-13}
$Sc_2(WO_4)_3$	Sc^{3+}	2.14×10^{-5}	1.72×10^{-14}

1.4. Conclusions

The trivalent cation conduction in $Sc_2(WO_4)_3$ type structure was estimated by the measurement of the potential energy around Al and W in $Al_2(WO_4)_3$ single crystal, the calculation of the electrostatic forces between migrating trivalent cation and surrounding ions in the $Sc_2(WO_4)_3$ structure, and the diffusion coefficient of Sc^{3+} ion. All data strongly support the trivalent cation conduction in $Sc_2(WO_4)_3$ type solid electrolyte, and the significant effect of the cation appearance whose valence state higher than trivalent is also clarified for trivalent cation conduction. Furthermore, anisotropic conducting behavior along each axis direction was explained by comparing the electrostatic forces among each conducting plane. The results obtained in this Chapter provide us a useful information for developing new series of multivalent cationic conductors.

Chapter 2

Trivalent R^{3+} Cation Conduction in $R_{1/3}Zr_2(PO_4)_3$ (R : Rare Earths) with the NASICON Type Structure

2.1. Introduction

Recently, $R_2(WO_4)_3$ (R : Al, Sc, Y, Lu–Er) solid electrolytes with the $Sc_2(WO_4)_3$ type structure have been reported as pure trivalent cationic conductors. The $Sc_2(WO_4)_3$ type structure is the quasi–layered and contains hexavalent tungsten ion, W^{6+}, which is strongly bonded to surrounding oxide anions comprising the framework resulting in reducing the electrostatic interaction between migrating trivalent R^{3+} cation and oxide anions. Furthermore, because the valence states of all cations in the structure are higher than three, no monovalent or divalent cation conduction appears and the R^{3+} conduction in the $R_2(WO_4)_3$ was directly and quantitatively demonstrated. However, the $R_2(WO_4)_3$ has a disadvantage both that W^{6+} cation which contributes for the trivalent cation migration in solids might be reduced to lower valence state not only by reducing atmosphere but also reacting with metals, resulting in an appearance of electronic conduction which greatly deteriorates ionic conducting characteristics and that the relative density of these tungstates are low not to utilize for applications.

It is necessary for realizing the pure trivalent cation conduction in solid that both the cation with higher valence state than three in the structure and the structure with enough pathway for ion conduction revealed in Chapter 1.

The NASICON is the solid electrolyte, which contains cations with high valence state such as P^{5+} and Zr^{4+} and possesses the three–dimensional network structure suitable for ion conduction, and the high Na^+ conductivity is also well known. Recently, $Ln_{1/3}Zr_2(PO_4)_3$ (Ln : lanthanoids) with the NASICON type structure were reported as new phosphates by Talbi et al. and the thermal property

of them was studied [44]. However, the Ln^{3+} cations contained in these materials are limited to some lanthanoid atoms and ionic conducting characteristics of them were not investigated at all. We selected the NASICON type structure as the lattice structure candidate, and selected the trivalent rare earth ions as the migrating cation species.

In this Chapter, the $R_{1/3}Zr_2(PO_4)_3$ (R : Sc, Eu, Gd, Er, Lu) phosphates were prepared by a sol–gel method and trivalent cation conducting properties in these solid electrolytes were studied.

2.2. Experimental Details

2.2.1. Materials

$R_{1/3}Zr_2(PO_4)_3$ phosphates were prepared by a sol–gel method from high purity R_2O_3 (99.9%), $ZrO(NO_3)_2 \cdot 2H_2O$ (99%) and $(NH_4)_2HPO_4$ (99.99%) as the starting materials. R_2O_3 and $ZrO(NO_3)_2 \cdot 2H_2O$ were separately solved in 3N HNO_3 solution, and mixed each other afterwards. Then $(NH_4)_2HPO_4$ solution (3%) was dropped into the mixed HNO_3 solution. After white precipitation were obtained, the solution was heated at 75 °C for 24h, then water in the solution was vaporized by heating at 130 °C for 6h. The dried precipitant was heated at 300 °C for 6h and the white powder obtained was pelletized and sintered at 850 °C for 12h. The sample characterization was done by X–ray powder diffraction using Cu-Kα radiation (M18XHF, Mac Science). The XRD data were collected by a step scanning method for the 2θ range between 10° and 70° with a step width 0.02° and a scan time 4s.

The densities of the powder and the sintered sample were measured by the gas pycnometer (Accupyc 1330, Micromeritics). The Vickers hardness of the sintered pellets was tested by using the Micro Hardness Tester (HMV-2, Shimadzu).

2.2.2. Electrical Measurements

Pt electrodes were sputtered on both center surfaces of the sample pellet. The ac conductivity of the sample was measured by a complex impedance method using the Precision LCR meter (Hewlett Packerd) in the frequency range between 20 Hz and 1MHz at the temperature range from 350 to 600 °C in air. The dc conductivity was obtained by the calculation from the voltage, the applied current, the surface area and the thickness of the sample and the polarization behavior was investigated by measuring the time dependence of the σ_{dc}/σ_{ac} ratio. The oxygen partial pressure dependencies of the electrical conductivity was measured in the oxygen pressure between 10^{-12} and 10^{5} Pa. Furthermore, oxygen–air concentration cell (2.1) described below was fabricated and the EMF generated was measured at the temperature range from 650 to 850 °C.

$$Pt, O_2 (Po_2 = 1 \times 10^5 Pa) \mid Sc_{1/3}Zr_2(PO_4)_3 \mid Air (Po_2 = 2.1 \times 10^4 Pa), Pt \qquad (2\text{-}1)$$

The electrolysis of the sample pellet was performed by applying a dc voltage of 3 V at 750 °C for 400 h for the purpose of identifying the conducting species, and the investigation of the cathodic surface of the sample after electrolysis was done by scanning electron microscope (SEM, S-800, HITACHI) measurements and electron probe micro-analysis (EPMA-1500, Shimadzu).

2.3. Results and discussion

2.3.1. Materials

All the $R_{1/3}Zr_2(PO_4)_3$ (R : Sc, Eu, Gd, Er, Lu) prepared were found to possess the NASICON type structure with hexagonal symmetry from the XRD measurements. Figure 2.1 shows the R^{3+} radius dependencies of the lattice parameters of the $R_{1/3}Zr_2(PO_4)_3$. As increasing the R^{3+} cation radius, a-axis increases and c-axis decreases monotonously, resulting in the lattice volume was found to increase.

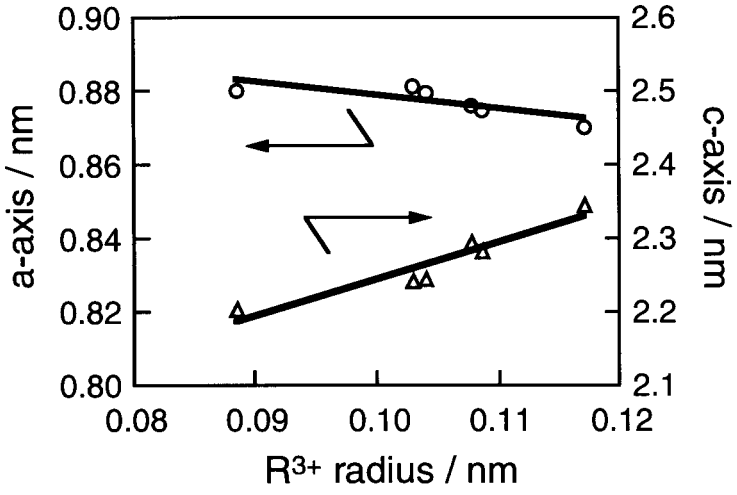

Figure 2.1. The R^{3+} radius dependencies of the lattice constant for the $R_{1/3}Zr_2(PO_4)_3$.

For utilizing the solid electrolyte to applications, both the high chemical and physical stability were required. $R_{1/3}Zr_2(PO_4)_3$ contains Zr^{4+} and P^{5+} in which these ion species have been already demonstrated to hold tetra– and pentavalent state stably and are extremely difficult to reduce.

The relative density and Vickers hardness of the $R_{1/3}Zr_2(PO_4)_3$ sintered pellet was listed in Table 2.1 with the corresponding data of the $Sc_2(WO_4)_3$ which had demonstrated as the Sc^{3+} conductor. All the $R_{1/3}Zr_2(PO_4)_3$ samples prepared show the high relative density and Vickers hardness and the highest values are obtained for $Sc_{1/3}Zr_2(PO_4)_3$ which has most suitable lattice size for trivalent cation conduction in the Phosphate with NASICON type structure as described below. The Vickers hardness of $Sc_{1/3}Zr_2(PO_4)_3$ was 293 Hv which was 7.3 times higher than that of $Sc_2(WO_4)_3$ and the relative density of the $Sc_{1/3}Zr_2(PO_4)_3$ is as high as 99.9%. Therefore, since the $R_{1/3}Zr_2(PO_4)_3$ have high chemical and physical stability, these solid electrolytes are found to be appropriate for various applications in comparison with the $Sc_2(WO_4)_3$ type.

Table 2.1. Relative density and Vickers hardness of the Sc^{3+} conductors.

Solid Electrolyte	Relative Density (%)	Vickers Hardness (Hv)
$Sc_{1/3}Zr_2(PO_4)_3$	99.9	293
$Sc_2(WO_4)_3$	89.0	40

2.3.2. Electrical Properties

For monovalent Li^+ ion conductor with the NASICON type structure, the existence of the most appropriate lattice size for Li^+ ion conduction has been clarified by Aono et al. [45] and they reported the detail of the relationship between the conducting Li^+ ion size and the lattice volume of LISICON (Li^+ super ionic conductor) with the NASICON type structure. Among $LiM_2(PO_4)_3$ (M=Ge, Ti, Hf) with the NASICON type structure, the $LiTi_2(PO_4)_3$ solid electrolyte is verified to have the suitable lattice size for Li^+ ion conduction. An optimum ratio of the conducting Li^+ ion size to the lattice volume in the NASICON type structure is calculated to be ca. 2.33×10^{-3} for $LiTi_2(PO_4)_3$.

Figure 2.2 shows the (R^{3+} volume / lattice volume) ratio (*A* ratio) of the $R_{1/3}Zr_2(PO_4)_3$ with the corresponding datum of $LiTi_2(PO_4)_3$ solid electrolyte (2.33×10^{-3}). In the case of trivalent cationic conduction, the electrostatic interaction between R^{3+} and surrounding oxide anions would be stronger than the case for monovalent Li^+ ion conduction. Therefore, the suitable lattice size for R^{3+} migration should be obtained for the solid electrolyte with the smaller *A* ratio compared with that ratio of the monovalent Li^+ conductor. Since only the $Sc_{1/3}Zr_2(PO_4)_3$ has the smaller *A* ratio of 1.97×10^{-3} than that of Li^+ (2.33×10^{-3}) which is lined as a broken line in Fig. 2.2, among $R_{1/3}Zr_2(PO_4)_3$, the highest conductivity is expected for Sc^{3+}.

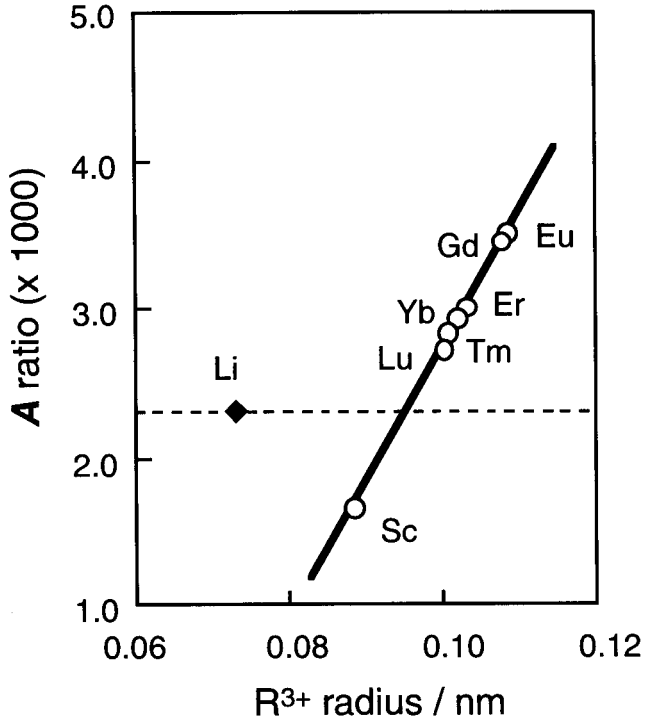

Figure 2.2. The relationship between the migrating ion radius and the migrating ion volume/the lattice volume ratio(A).

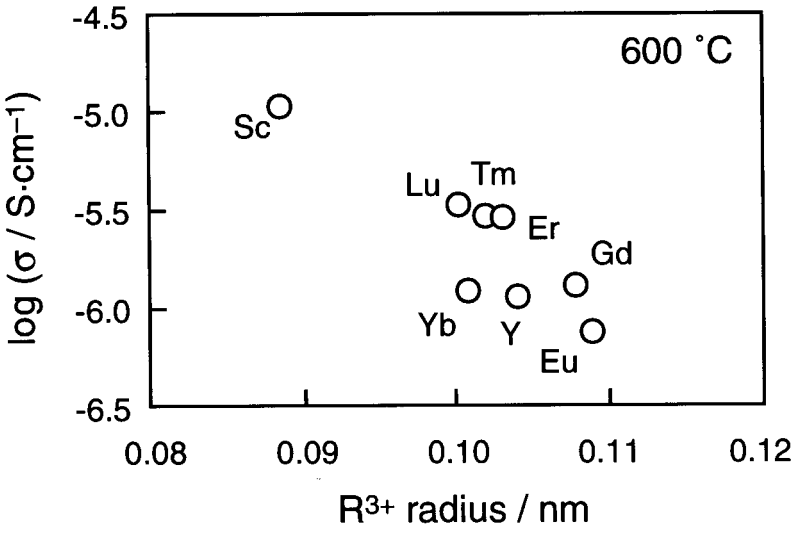

Figure 2.3. R^{3+} radius dependencies of the electrical conductivity for the $R_{1/3}Zr_2(PO_4)_3$ at 600 °C.

The trivalent R^{3+} radius dependencies of the electrical conductivity for the $R_{1/3}Zr_2(PO_4)_3$ at 600 °C are shown in Figure 2.3. As speculated from the above mentioned *A* ratio variation of $R_{1/3}Zr_2(PO_4)_3$, the conductivity monotonously increased with decreasing the R^{3+} ion size, and the $Sc_{1/3}Zr_2(PO_4)_3$ showed the highest conductivity of 1.06 x 10^{-5} S·cm^{-1}. Figure 2.4 presents the temperature dependencies of the electrical conductivity for $Sc_{1/3}Zr_2(PO_4)_3$ with those of $Sc_2(WO_4)_3$ and $Al_2(WO_4)_3$, which show the highest and the lowest trivalent ion conductivity among the $Sc_2(WO_4)_3$ type solid electrolytes. $Sc_{1/3}Zr_2(PO_4)_3$ shows a comparable conductivity to the tungstate series and the conductivity at 600 °C (1.06 x 10^{-5} S·cm^{-1}) is 2.5 times higher than that of $Al_2(WO_4)_3$ ($\sigma_{600°C}$= 4.27 x 10^{-6} S·cm^{-1}). Although we tried to prepare the $Al_{1/3}Zr_2(PO_4)_3$ which is expected to

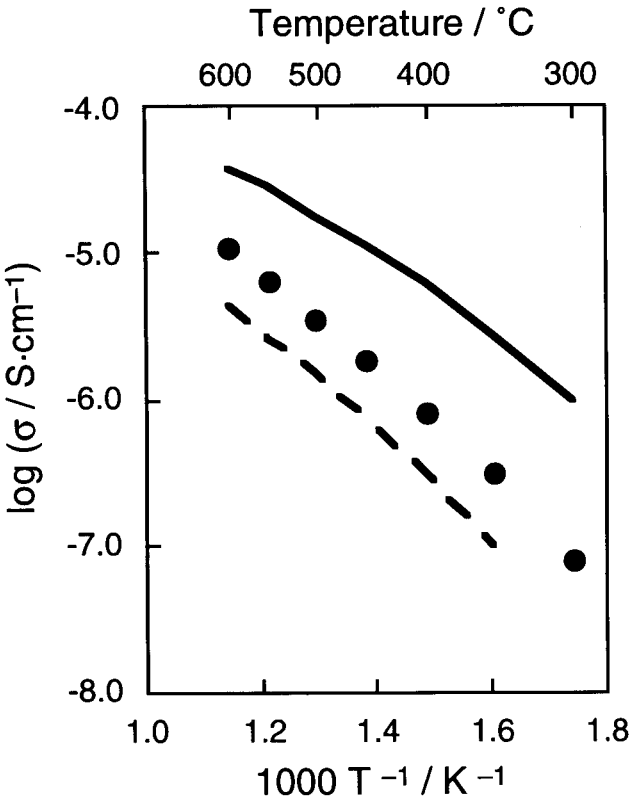

Figure 2.4. Temperature dependencies of the electrical conductivity for the $Sc_{1/3}Zr_2(PO_4)_3$ (●), $Sc_2(WO_4)_3$ (—), and $Al_2(WO_4)_3$ (- -).

have more small *A* ratio than the $Sc_{1/3}Zr_2(PO_4)_3$, the sample obtained was a two phase mixture of $AlPO_4$ and ZrP_2O_7 because the Al^{3+} radius is too small to hold the NASICON type structure, so that the $Sc_{1/3}Zr_2(PO_4)_3$ was found to possess the highest conductivity among the $R_{1/3}Zr_2(PO_4)_3$ with NASICON type structure.

Figure 2.5 depicts the oxygen partial pressure dependence of the ac conductivity for the $Sc_{1/3}Zr_2(PO_4)_3$ at 700 °C. No meaningful deviation of the ac conductivity was observed for the whole oxygen pressure region measured, which indicates that the predominant charge carrier is only ion and neither electron nor hole. Figure 2.6 shows the dc to ac conductivity ratio as a function of time in O_2 (Po_2 = 10^5 Pa) and He (Po_2 = 4 Pa) atmosphere at 700 °C for $Sc_{1/3}Zr_2(PO_4)_3$ solid electrolyte. In the case for the O^{2-} ion conductor, the dc conductivity is same value as the ac one in O_2 atmosphere since the conducting O^{2-} ion can be provided from the O_2 gas atmosphere, and the σ_{dc}/σ_{ac} ratio holds the value of one constantly. In contrast, the σ_{dc}/σ_{ac} ratio decreases in low O_2 pressure such as He where O^{2-} ion can not be supplied enough into the solid electrolyte and a clear

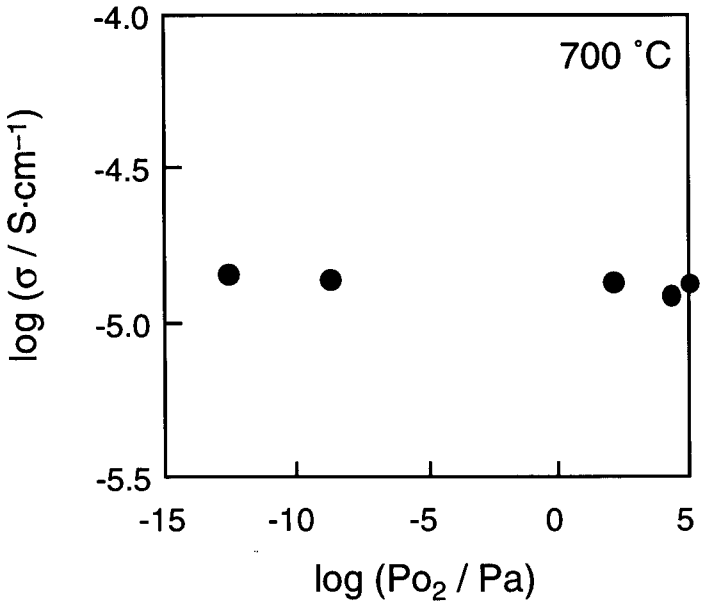

Figure 2.5. The oxygen pressure dependence of the ac conductivity for $Sc_{1/3}Zr_2(PO_4)_3$ at 700 °C.

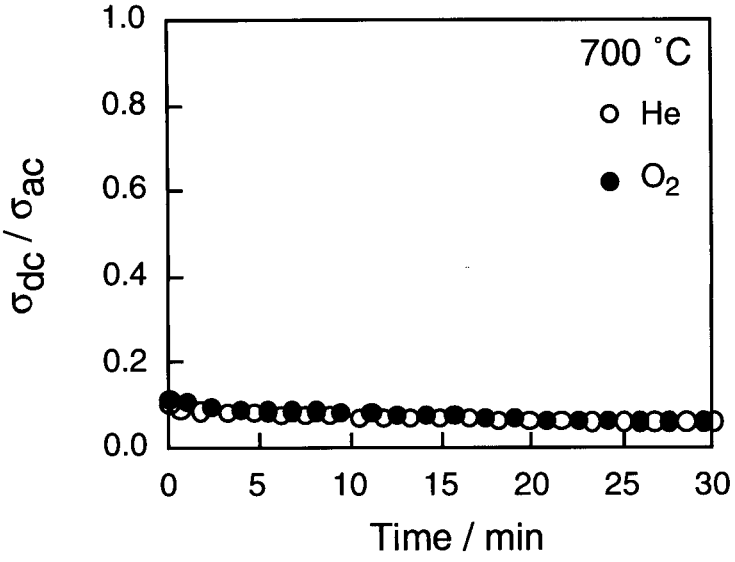

Figure 2.6. The time dependence of the dc to ac conductivity ratio for $Sc_{1/3}Zr_2(PO_4)_3$ at 700 °C.

polarizing behavior would be observed. It shows an abrupt decrease in the σ_{dc}/σ_{ac} ratio for both O_2 and He atmospheres, and this result is definitely different from that of oxide anion conductors [25], indicating no O^{2-} ion migration in the $Sc_{1/3}Zr_2(PO_4)_3$ solid electrolyte.

Furthermore, oxygen–air concentration cell (2-1) was fabricated and the EMF generated was measured at the temperature range from 650 to 850 °C. The theoretical EMF values of this concentration cell (2-1) were calculated from the following Nernst equation (2-2):

$$E = -(RT)/(4F)\ln(Po_2''/Po_2') \qquad (2\text{-}2)$$

where F is Faraday constant. The measured and the theoretical EMF were shown in Figure 2.7. The measured EMF was coincided well to the theoretical value of Nernst equation (2-2). The current frown is lower than the theoretical value in the case of the electronic conductor, and the constant current was drown out in the case of the oxide anion conductor. The oxygen–air concentration cell with $Sc_{1/3}Zr_2(PO_4)_3$ was not be able to draw out the constant current, therefore, this result also supports that the predominant charge carrier is cationic in $Sc_{1/3}Zr_2(PO_4)_3$.

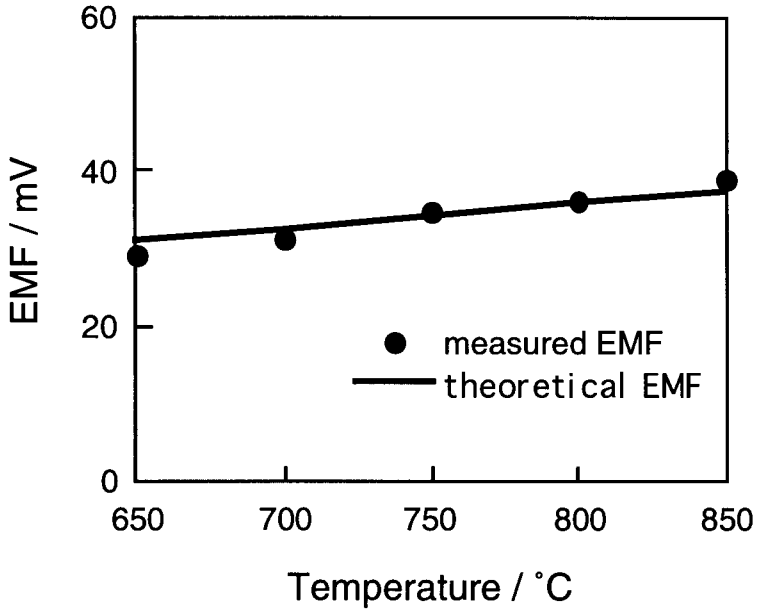

Figure 2.7. The temperature dependencies of the EMF for $Sc_{1/3}Zr_2(PO_4)_3$ of the oxygen–air concentration cell. Solid line shows the theoretical EMF.

2.3.3. DC Electrolysis

The dc electrolysis is one of direct identifying methods of conducting species. In the case for electron or hole conductors, the electron and hole migrate by applying a dc voltage and the no change of the sample was recognized because these species migrate into electrolyte without decomposing the sample. On the other hand, for the case of ionic conductors, the sample was decomposed by applying higher dc voltage than the decomposition voltage and the ion which generated by the decomposition can migrate in solid electrolyte. However, since the ions can not move in the electrode, the surface of the sample where contacted with electrode should change.

For the purpose of identifying the migrating cation species in $Sc_{1/3}Zr_2(PO_4)_3$, a dc electrolysis which can directly determine the conducting species in solid electrolytes was performed using two Pt bulk as blocking electrodes at 700 °C (The decomposition voltage of the $Sc_{1/3}Zr_2(PO_4)_3$ solid electrolyte had been preliminary measured at 700 °C and is determined to be ca. 2 V.).

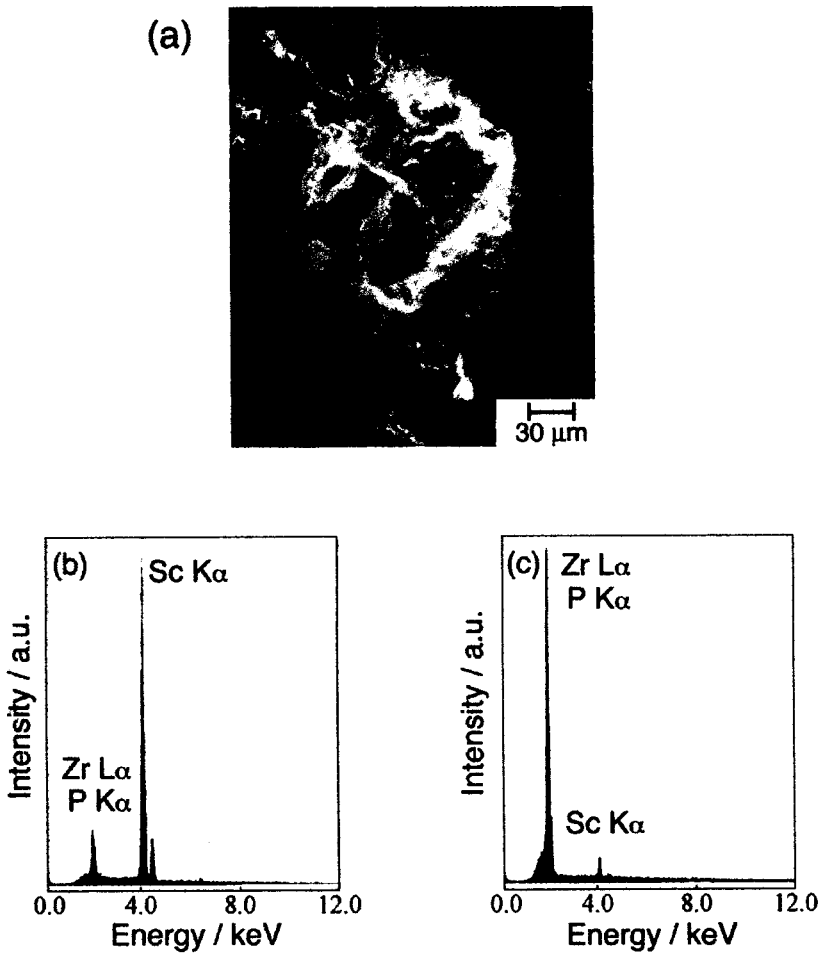

Figure 2.8. (a) The SEM photograph of the deposit on cathodic surface of the $Sc_{1/3}Zr_2(PO_4)_3$ pellet after the electrolysis and the results of the EPMA spot analysis of the cathodic surface (b) after and (c) before the electrolysis.

By applying a dc voltage of 3 V which is higher than the decomposition voltage at 700 °C, the conducting cation species should migrate successively from the anode to the cathode direction and deposits on the cathodic surface which is in contact with the Pt blocking electrode. After the electrolysis, deposits were recognized at only cathodic surface and depicted in Figure 2.8(a). From the EPMA spot analysis, the Sc/(Sc+Zr+P) ratio in the deposit increased approximately 7.6 times as high as that in the bulk before electrolysis as shown in Fig. 2.8(b). These results explicitly indicate that the Sc^{3+} ions macroscopically migrate from anode to cathode direction by applying a dc voltage and deposit on the cathodic surface, thus, the mobile cationic species in $Sc_{1/3}Zr_2(PO_4)_3$ is directly identified to be Sc^{3+} ion.

Conclusions

The $R_{1/3}Zr_2(PO_4)_3$ with NASICON type structure was newly developed by a sol–gel method with an aim of the improvement of the demerits in which $Sc_2(WO_4)_3$ type tungstates have. The suitable lattice size for trivalent R^{3+} ion conduction in $R_{1/3}Zr_2(PO_4)_3$ with NASICON type structure was obtained for $Sc_{1/3}Zr_2(PO_4)_3$ which is composed of the smallest trivalent cation of Sc^{3+} among the rare earth series. With decreasing the R^{3+} size in the $R_{1/3}Zr_2(PO_4)_3$, the trivalent ion conductivity monotonously increased, and the $Sc_{1/3}Zr_2(PO_4)_3$ shows the highest conductivity which is comparable value of that for the $Sc_2(WO_4)_3$ type solid electrolyte series.

Since the $R_{1/3}Zr_2(PO_4)_3$ solid electrolyte is chemically stable enough in addition to holding the high ion conductivity comparable to that of the $Sc_2(WO_4)_3$ type trivalent cationic conductors, the utilization for various electrical devices applicable from in oxidizing to reducing atmosphere is greatly expected.

Chapter 3

$R_{1/3}Zr_2(PO_4)_3$ Prepared by a Solid–State Reaction with Ball Milling Method

3.1. Introduction

The $R_{1/3}Zr_2(PO_4)_3$ with NASICON type structure prepared by a sol–gel method were clearly demonstrated to be new trivalent R^{3+} cationic conductors in Chapter 2. The $R_{1/3}Zr_2(PO_4)_3$ have both the high chemical and the high mechanical stability compared to the $Sc_2(WO_4)_3$ type trivalent cation conductors. However, the conductivity of the samples prepared by a sol–gel method was the lower than that for $Sc_2(WO_4)_3$. In order to enhance the conductivities of $R_{1/3}Zr_2(PO_4)_3$ solid electrolytes, it is most effective to improve the low crystallinity and to create the well–ordered three–dimensional conducting pathways in the grains. However, the crystallization and the decomposition temperatures of the samples prepared by a sol–gel method are very close, and the improvement of the crystallinity seemed to be difficult by preparation from sol–gel method.

The reaction among the very small particles is well known to readily occur due to the high surface area. However, the $R_{1/3}Zr_2(PO_4)_3$ solid electrolytes could not be obtained by a conventional solid–state reaction might be owing to the relatively large powder in size as described in Chapter 2. Thus, we tried to crush the powder by using a ball milling method. In addition, the premilled powder is an amorphous state by giving the strong mechanical force. In general, amorphous state is a metastable phase and the activation energy necessary for the reaction of the product formation is reduced in comparison with the case for the reaction by a conventional solid–state method.

In this Chapter, the $R_{1/3}Zr_2(PO_4)_3$ solid electrolytes were prepared by a solid–state reaction with a ball milling method and those electrical conducting properties were discussed.

3.2. Experimental Details

3.2.1. Sample Preparation

Reagent grade of R_2O_3 (99.9%), $ZrO(NO_3)_2 \cdot 2H_2O$ (99%), and $(NH_4)_2HPO_4$ (99.9%) were mixed in an agent pot at a rotation speed of 300 rpm for 12h. After checking the resulting powder to be an amorphous state by the XRD measurement, the powder obtained was made into pellet (10 mm in diameter) and sintered on a aluminum plate at between 850 and 950 °C for 12h in air.

Thermogravimetric and differential thermal analysis measurements (DTG–50, Shimadzu CO. Ltd.) were performed up to 1200 °C at a heating rate of 5 °C/min.

3.2.2. Electrical Conducting Measurements

The sintered pellets were polished with 2000 grade emery paper and platinum sputtered layer was formed on both center surfaces of the pellets in order to obtain a good contact with the electrode. Ac conductivity of the samples was measured by sandwiching the sample between two Pt electrodes at a temperature between 300 and 600 °C in a frequency range from 5Hz to 13MHz by using LCR meter (8284A, Hewlett Packard). The dc conductivity was obtained by the calculation from the voltage, the applied current, the surface area and the thickness of the sample.

For the purpose of identifying the charge carrier in the sample, the dc electrolysis was performed with two platinum plates as the blocking electrode by applying a voltage of 3 V for 150 h at 750 °C in air. After the electrolysis, SEM (SEM, S-800, HITACHI) observation and EPMA (EPMA-1500, Shimadzu) were carried out for the cathodic bulk surface.

3.3. Results and Discussion

3.3.1. Sample Crystallinity

All samples prepared by a ball milling method were found to hold the NASICON type structure similar to the case for the samples prepared by a sol–gel method from the XRD measurements. Figure 3.1 shows the XRD patterns of the $Sc_{1/3}Zr_2(PO_4)_3$, which was obtained by a ball milling method, before and after sintering process at 850 °C with a corresponding datum of the sample prepared by a sol–gel method. While the sample obtained by the ball milling method was in an amorphous state before sintering since the powder was mechanically milled with a strong force, the sample crystallized after sintering at 850 °C and its crystallinity was found to be improved compared to that of the sample obtained by the sol–gel method. In addition, the decomposition temperature of the sample with ball milling method also increased to ca. 950 °C from ca. 900 °C for the case of the sample prepared by the sol–gel method. As described in chapter 2, the NASICON type $R_{1/3}Zr_2(PO_4)_3$ solid electrolytes were not successfully obtained by a conventional solid–state

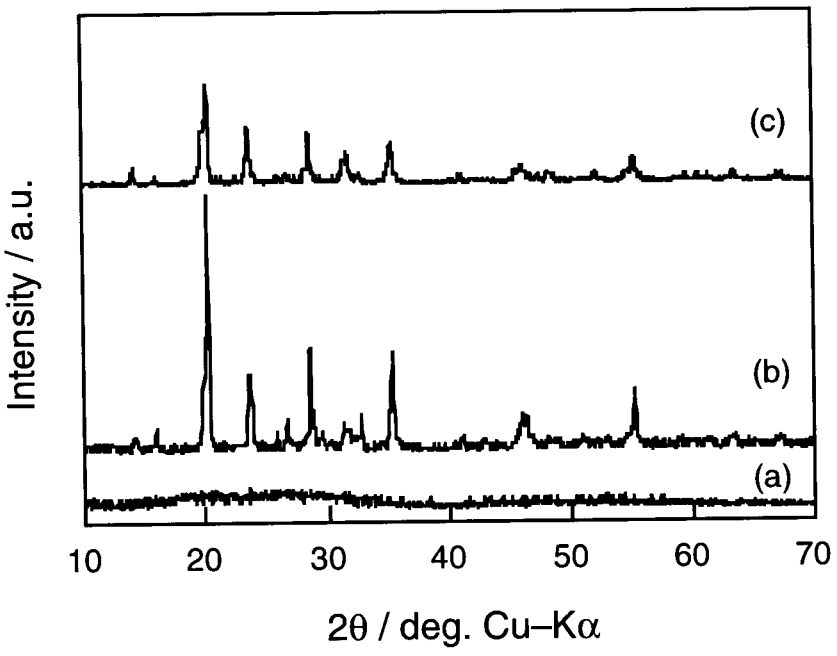

Figure 3.1. The XRD patterns of the $Sc_{1/3}Zr_2(PO_4)_3$ obtained by a ball milling method (a) before and (b) after sintering at 850 °C, and (c) by a sol–gel method.

reaction because the energy for the solid–state reaction was not enough and if the temperature is raised up to 950°C that is over decomposition temperature and the sample decomposed to $ScPO_4$ and ZrP_2O_7 over 950 °C. On the other hand, the sample prepared by a ball milling method was through the amorphous state of the metastable phase, and the energy level might be higher than that for the starting mixture. The activation energy necessary for the reaction from the metastable phase to the product is low in comparison with the case from the starting mixture, and the reaction is expected to occur easily at lower temperature (ca. 800 °C). In addition, the high crystallinity was obtained because the powder obtained by the ball milling method does not include water which is different form the case for the sample prepared by a sol–gel.

3.3.2. Electrical Conducting Properties

– $Sc_{1/3}Zr_2(PO_4)_3$ –

The temperature dependencies of the electrical conductivity for the $Sc_{1/3}Zr_2(PO_4)_3$ prepared by the ball milling method was shown in Figure 3.2 with the corresponding data of $Sc_{1/3}Zr_2(PO_4)_3$ obtained by the sol–gel method and $Sc_2(WO_4)_3$. The conductivity of the sample prepared by the ball milling method was 2.91 x 10^{-5} $S \cdot cm^{-1}$ which was 3.2 times as high as that for the sample prepared by the sol–gel method (9.07 x 10^{-6} $S \cdot cm^{-1}$) and the conductivity reached the comparable value of the $Sc_2(WO_4)_3$ (3.74 x 10^{-5} $S \cdot cm^{-1}$) at 600 °C. Furthermore, the activation energy for ion conduction prepared by the ball milling method was 59.5 $kJ \cdot mol^{-1}$, which was lower than that for the sample prepared by the sol–gel method (67.8 $kJ \cdot mol^{-1}$). The enhancement of the conductivity and redaction of the activation energy for the $Sc_{1/3}Zr_2(PO_4)_3$ was caused by the improvement of the crystallinity of the sample.

In order to identify the conducting ion species in $Sc_{1/3}Zr_2(PO_4)_3$ prepared by the ball milling method, the dc electrolysis was carried out at 700 °C. The SEM photograph at the cathodic surface of the $Sc_{1/3}Zr_2(PO_4)_3$ and the EPMA measurement result are shown in Figure 3.3. A lot of deposits were observed (Figure 3.3. (a)) and the Sc amount in the deposit (Figure 3.3 (b)) was found to

increase ca. 5.6 times as high as that for the sample before electrolysis (Figure 3.3 (c)) by EPMA. The results clearly indicate that $Sc_{1/3}Zr_2(PO_4)_3$ prepared by the ball milling method was the Sc^{3+} ion conductor same as the sample prepared by the sol–gel method described in Chapter 2. In addition, the other experiment such as the oxygen pressure dependencies of the conductivity and dc conductivity deviation in various atmospheres such as oxygen and helium were also done and the same results as the case for the sample with the sol–gel method were obtained.

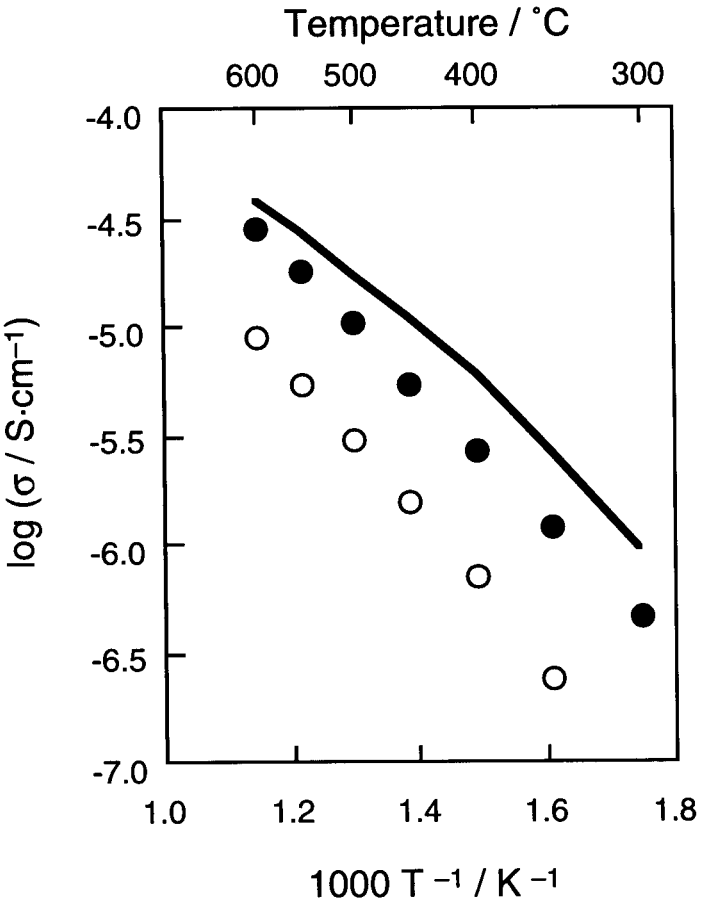

Figure 3.2. Temperature dependencies of the electrical conductivity for the $Sc_{1/3}Zr_2(PO_4)_3$ prepared by the ball milling method(●) and by the sol–gel method (○), and $Sc_2(WO_4)_3$ (—).

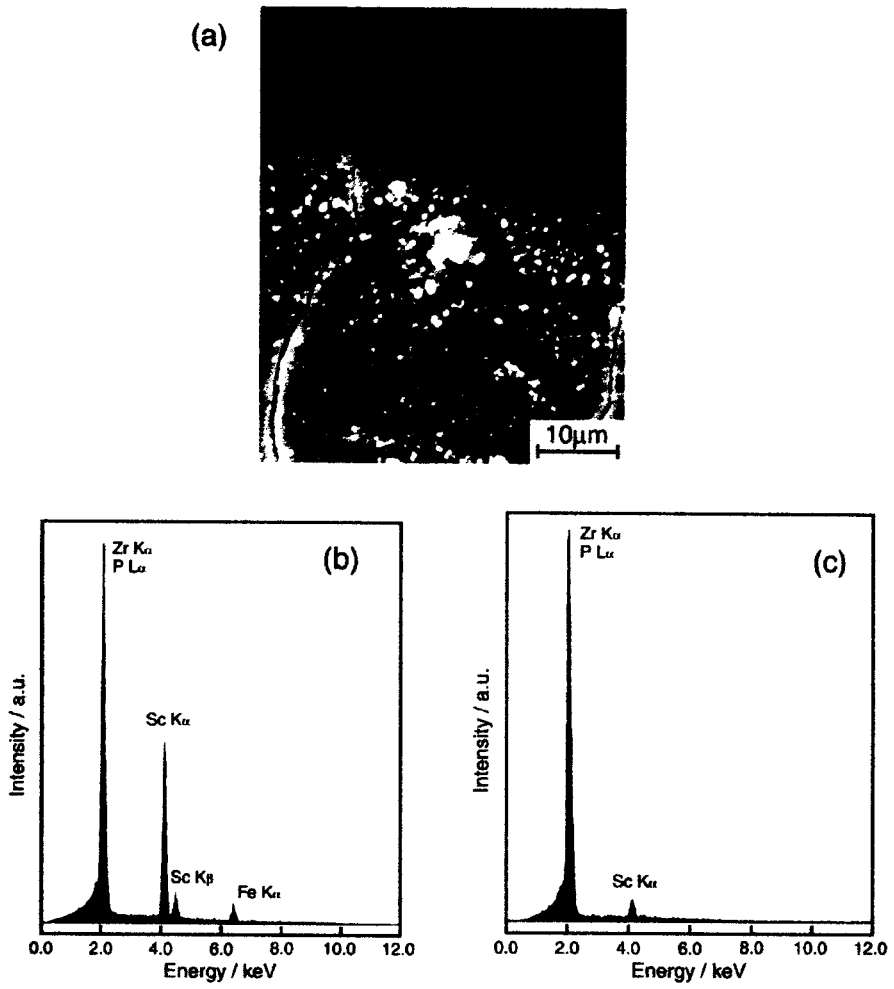

Figure 3.3. (a) The SEM photograph of the deposit on cathodic surface of the $Sc_{1/3}Zr_2(PO_4)_3$ pellet after the electrolysis and the results of the EPMA spot analysis of the cathodic surface (b) after and (c) before the electrolysis.

– $R_{1/3}Zr_2(PO_4)_3$ –

The ball milling method was also applied for the samples contains other trivalent cation, R (R= Y, Er, Tm, Lu). Figure 3.4 depicts the R^{3+} radius dependencies of the conductivity at 600 °C for $R_{1/3}Zr_2(PO_4)_3$ with the corresponding data of $Sc_{1/3}Zr_2(PO_4)_3$. The corresponding data of the samples prepared by the sol–gel method were also shown in same figure. The conductivity of the samples with ball milling method was enhanced about 3 times as high as that for the samples prepared by the sol–gel method. The temperature dependence of the electrical conductivity for $Tm_{1/3}Zr_2(PO_4)_3$ is depicted in Figure 3.5 as one of representative results. The activation energy for the case of $Tm_{1/3}Zr_2(PO_4)_3$ (53.5 $kJ \cdot mol^{-1}$) was lowered in comparison with the sample prepared by the sol–gel method (64.9 $kJ \cdot mol^{-1}$). The result that the activation energy for the Tm system was also reduced similar to the case for Sc system indicates that the ball milling method is one of suitable preparation methods for such a sample can not be crystallized owing to the low decomposition temperature.

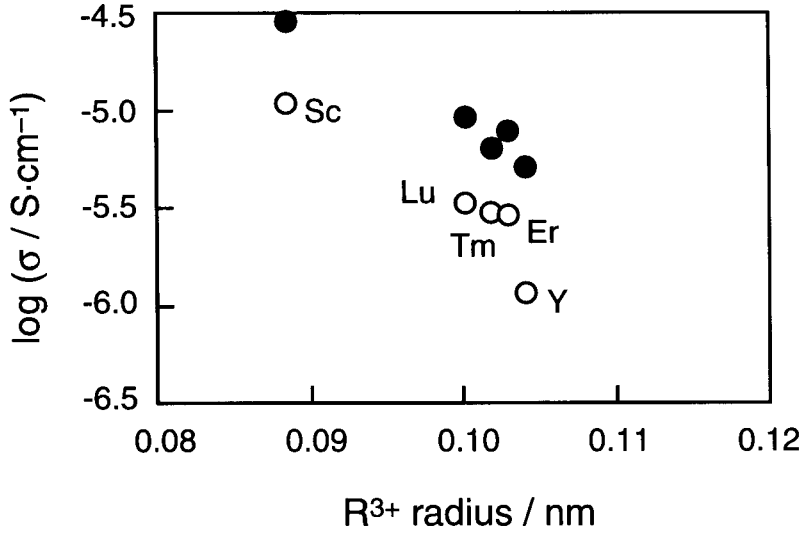

Figure 3.4. R^{3+} radius dependencies of the electrical conductivity for $R_{1/3}Zr_2(PO_4)_3$ prepared by the ball milling method (●) and the sol–gel method (○) at 600 °C.

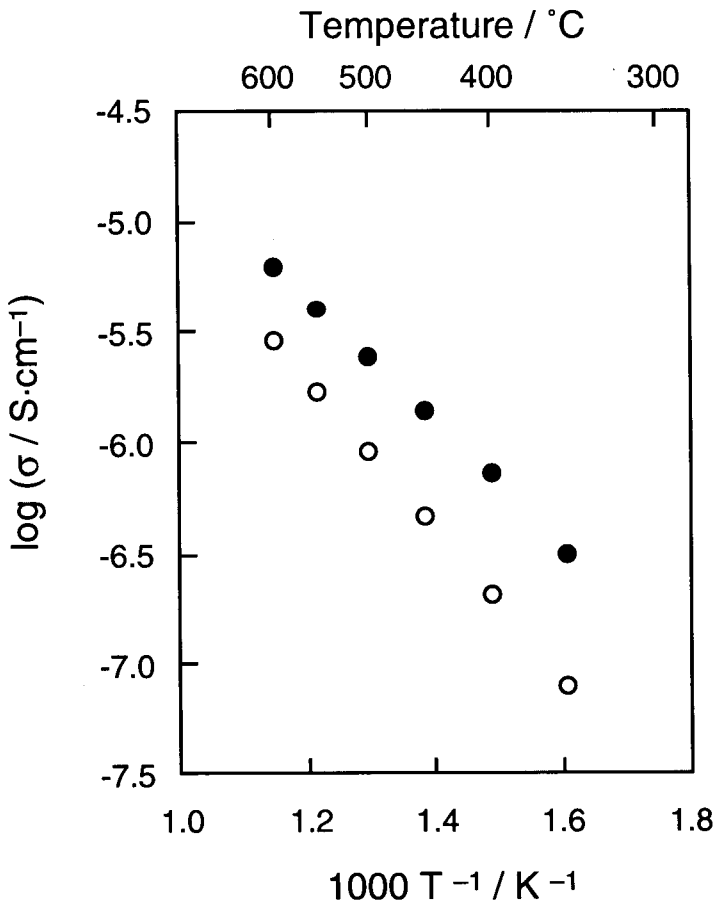

Figure 3.5. Temperature dependencies of the electrical conductivity for the $Tm_{1/3}Zr_2(PO_4)_3$ prepared by the ball milling method (●) and by the sol–gel method (○).

3.4. Conclusions

The $R_{1/3}Zr_2(PO_4)_3$ with NASICON type structure was prepared by a ball milling method with an aim of enhancing the crystallinity of the sample. The conductivity of the $R_{1/3}Zr_2(PO_4)_3$ increased about 3 times and the activation energy for trivalent ion conduction was reduced in comparison with that of the sample prepared by the sol–gel method, and the conductivity of the $Sc_{1/3}Zr_2(PO_4)_3$ is equivalent to the value of $Sc_2(WO_4)_3$, which is the highest conductivity in the tungstate solid electrolyte series. The formation of the well–ordered three–demensional conducting pathway obtained by the metastable amorphous phase results in the enhancement of the

conductivity and reduction of the activation energy.

The ball milling method is one of great advantages in preparing the sample whose easily decompose temperature is too low to obtain by a conventional solid–state reaction method.

Chapter 4.

A CO_2 sensor based on a Sc^{3+} conducting $Sc_{1/3}Zr_2(PO_4)_3$ solid electrolyte

4.1. Introduction

In these years, a global warming mainly caused by emitted CO_2 gas has been becoming a very serious problem and the effective suppression of CO_2 generated in various industrial fields has been greatly required. In order to reduce the CO_2 gas amount emitted into the atmosphere, the on-site monitoring and the controlling of CO_2 generated at each emitting site are greatly requested. For accomplishing this target, the commonly utilized methods such as infrared spectroscopy are not suitable because the size is too large to set up at every detecting site. Therefore, compact sensors which can be installed at every detecting site are strongly desired. As the candidates of the compact CO_2 sensor component, semiconducting [46-48] and solid electrolyte [49-53] materials are proposed. However, the sensor with semiconductors can not avoid the interference of the gas species other than CO_2 since their detecting mechanism is based on the gas adsorption on the semiconductor surface. In contrast, solid electrolytes have a unique characteristic that only one ion species can migrate in solids and are used for various practical applications such as oxygen gas sensors based on yttria stabilized zirconia(YSZ) and lithium batteries for heart pacemaker etc. Up to now, various types of compact CO_2 sensors based on alkali metal ion conducting solid electrolytes have been proposed. Among them, the sensors based on Li^+ ion conducting solid electrolyte and YSZ with Li_2CO_3 as an auxiliary electrode are reported to exhibit a high sensing performance [52, 53]. However, this sensor still have a critical problem of the low stability in sensor's output. The CO_2 concentration was determined by the EMF output which strongly depends on the chemical activity of Li_2O formed at the interface between two solid electrolytes of the Li^+ ion conductor and YSZ. Li_2O is considerably unstable and once cracks appear in the sensor

cell, Li_2O reacts with water vapor and CO_2 in the atmosphere to form LiOH and Li_2CO_3, resulting in a considerable deviation of the sensor output. In order to overcome the critical points mentioned above, a new type of CO_2 sensor using trivalent Sc^{3+} ion conducting solid electrolyte ($Sc_2(WO_4)_3$) for the Li^+ ion conductor was proposed [54]. The $Sc_2(WO_4)_3$ electrolyte has an advanced merit to possess the highest trivalent ion conductivity among the tungstate solid electrolytes with $Sc_2(WO_4)_3$ type structure. The sensor output based on the $Sc_2(WO_4)_3$ electrolyte is very stable because the EMF depends on the activity of the stable oxide of Sc_2O_3 formed at the interface between $Sc_2(WO_4)_3$ and YSZ. However the hexavalent tungsten ion existing in $Sc_2(WO_4)_3$ is thought to be reduced to a lower valent state in a reducing atmosphere. As a result, an electronic conduction appears and seriously deteriorates the sensing characteristics. Furthermore, since the sinterability of the $Sc_2(WO_4)_3$ electrolyte is appreciably low, Li_2CO_3 used as the auxiliary electrode permeates into the polycrystalline $Sc_2(WO_4)_3$ pellet and the permeation makes $Sc_2(WO_4)_3$ fragile and weakens the mechanical strength of the pellets. In the worst case, Li_2CO_3 reaches the interface between $Sc_2(WO_4)_3$ and YSZ, and the cell can not work as a sensing tool any more. In order to realize a compact CO_2 sensor with a high sensitivity and a long–term stability, both a high chemical stability and a high mechanical strength are required for the solid electrolyte to be applied for practical sensors in addition to the formation of stable oxides between two electrolytes.

In this chapter, we select the $Sc_{1/3}Zr_2(PO_4)_3$, which has a high mechanical strength in addition to the highest trivalent ion conductivity among the $R_{1/3}Zr_2(PO_4)_3$ as described in chapter 2, as the component of present sensor. A compact CO_2 sensor was fabricated with the $Sc_{1/3}Zr_2(PO_4)_3$, and an excellent sensing performance with a long–term stability was demonstrated here.

4.2. Experimental Details

4.2.1. Sample Preparation

Yttria stabilized zirconia (YSZ) was prepared by a conventional solid state reaction from reagent grade of Y_2O_3(99.9%) and ZrO_2(99.9%). After mixing ZrO_2 and Y_2O_3 in a molar ratio of 9:1 in a mortar, the mixed powder was heated at 1600 °C for 6h two times. The obtained powder was pelletized and sintered at 1600 °C for 12h.

The characterization of YSZ was done by X-ray powder diffraction using Cu-Kα radiation (M18XHF, Mac Science). The XRD data were collected by a step-scanning method for the 2θ range from 10° to 70° with a step width 0.04° and a scan speed of 10°/min.

On the center surface (diameter: 6.2 mm) of the pellets, Pt layer was sputtered as the electrodes. Two solid electrolytes were fixed by an inorganic adhesive agent (SUMICERAM-17D, Asahi) as shown in Figure 4.1. The platinum and gold net were attached to the pellets as the reference and the detecting electrode, respectively. As the lead, Pt and Au wire were utilized. By heating the sensor element at 650 °C for 12h in a 5 vol% CO_2 diluted air, Li_2CO_3 was formed from $LiOCH_3$ which was attached on the $Sc_{1/3}Zr_2(PO_4)_3$ surface.

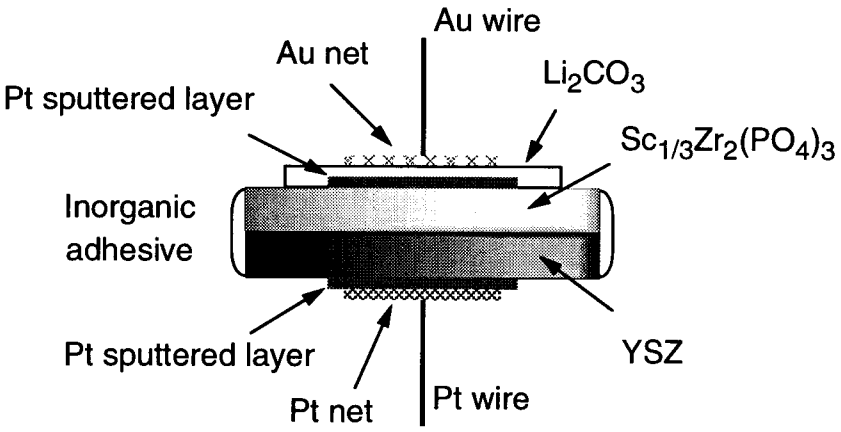

Figure 4.1. The cross sectional drawing of the sensor element based on $Sc_{1/3}Zr_2(PO_4)_3$ and YSZ with a Li_2CO_3 auxiliary electrode.

4.2.2. CO_2 sensing

EMF measurements were performed at 550 °C with the CO_2 concentration ranges from 200 to 2000 ppm and from 1 to 5 % which were regulated by mixing air – 1 vol% CO_2 diluted with N_2 or air – pure CO_2, respectively. The long–term stability of the sensor output was tested by monitoring the EMF outputs at 400 and 2000 ppm CO_2 every several days. The sensor cell was hold constant at 550 °C in dry air atmosphere during the experiment. The EMF measurements were also done in the atmosphere where NO (0 - 500 ppm), NO_2 (0 - 500 ppm), or O_2 (5 - 40%) coexist under the condition of the CO_2 concentration at 1 %. The CO_2 sensing characteristics were also studied in the air atmosphere where water vapor (4.2, 10, 30 vol%) coexists.

4.3. Results and discussion

As can be easily seen from Figure 4.1, the whole sensor element is inserted in the detecting atmosphere. The practical gas sensors should show a high sensing performance such as a high sensitivity and a high selectivity. In addition, the sensor must be also chemically stable to operate in such serious conditions where the atmosphere changes from a reducing to an oxidizing condition and vice versa since the oxygen pressure continuously changes in actual CO_2 detecting sites. The solid electrolytes applied for the sensor should have not only a chemical stability but also a physical stability, that is, a reasonably high sinterability to overcome the stress caused by the temperature and the humidity variation. Since the $Sc_{1/3}Zr_2(PO_4)_3$ utilized to present sensor has an appreciably high sinterability and a high mechanical strength compared with $Sc_2(WO_4)_3$ as described in chapter 2, Li_2CO_3 used as an auxiliary electrode did not penetrate into $Sc_{1/3}Zr_2(PO_4)_3$, while $Sc_2(WO_4)_3$ became ductile and many cracks appeared on the $Sc_2(WO_4)_3$ surface which was confirmed at a glance. Although the conductivity of the $Sc_{1/3}Zr_2(PO_4)_3$ is about one third lower than that of the $Sc_2(WO_4)_3$, the lower conductivity is not a disadvantage in the case of CO_2 sensing because the detecting mechanism of the present sensor is to monitor the potentiometric signal of the sensor

output generated from the difference in chemical activity between the detecting and the reference electrode as described below, and the current pass through the sensor element is negligibly low. In addition, $Sc_{1/3}Zr_2(PO_4)_3$ is based on chemically stable phosphate, any electronic conduction which results in the electronic short-circuit of solids would not be expected to appear even in a reducing atmosphere. Therefore, $Sc_{1/3}Zr_2(PO_4)_3$ is thought to be much more suitable candidate for solid electrolyte applied for CO_2 sensor compared with $Sc_2(WO_4)_3$ electrolyte from the view point of both chemical and physical stability. Furthermore, because the sensor fabricated with the $Sc_{1/3}Zr_2(PO_4)_3$ solid electrolyte forms a very stable oxide (Sc_2O_3) at the interface between $Sc_{1/3}Zr_2(PO_4)_3$ and YSZ (described below), the sensor based on $Sc_{1/3}Zr_2(PO_4)_3$ is greatly expected to exhibit a well stable sensor output.

The following reactions occur at the detecting electrode, the interface (Interface I) between detecting electrode and $Sc_{1/3}Zr_2(PO_4)_3$, the interface (Interface II) between $Sc_{1/3}Zr_2(PO_4)_3$ and YSZ, and at the reference electrode.

Detecting electrode:

$$Li_2CO_3 \rightarrow 2Li^+ + CO_2' + (1/2)O_2' + 2e^- \quad (4\text{-}1)$$

Interface I:

$$2Li^+ + 2Sc_{1/3}Zr_2(PO_4)_3 \rightarrow (2/3)Sc^{3+} + 2LiZr_2(PO_4)_3 \quad (4\text{-}2)$$

Interface II:

$$(2/3)Sc^{3+} + O^{2-} \rightarrow (1/3)Sc_2O_3 \quad (4\text{-}3)$$

Reference electrode:

$$(1/2)O_2'' + 2e^- \rightarrow O^{2-} \quad (4\text{-}4)$$

The total chemical reaction of the present sensor is written as

$$Li_2CO_3 + 2Sc_{1/3}Zr_2(PO_4)_3 + (1/2)O_2'' \rightarrow$$

$$(1/3)Sc_2O_3 + CO_2' + (1/2)O_2' + 2LiZr_2(PO_4)_3 \quad (4\text{-}5)$$

As the $Sc_{1/3}Zr_2(PO_4)_3$, Li_2CO_3 and the $LiZr_2(PO_4)_3$ formed at the interface I are supposed to be in a solid state, the activities $aSc_{1/3}Zr_2(PO_4)_3$, aLi_2CO_3 and $aLiZr_2(PO_4)_3$ are unity. Furthermore, the oxygen partial pressure at the detecting electrode (O_2') is exactly equal to that at the reference electrode (O_2'') because the present sensor element is inserted in the same atmosphere as illustrated in Figure 4.1. Then, the Nernst equation is described as

$$E = C_1(\text{constant}) - (RT/nF)\ln(aSc_2O_3)^{1/3}(PCO_2') \quad (n=2.00) \quad (4\text{-}6)$$

In eq.(4-6), aSc_2O_3 is constant because the Sc_2O_3 is highly stable at the operating temperature of 550 °C, and can be further simplified as

$$E = C_2(\text{constant}) - (RT/nF)\ln(PCO_2') \quad (n=2.00) \quad (4.7)$$

Figure 4.2 depicts one of representative sensor response curves in dry atmosphere. The time necessary for the attainment of 90% response was within 1 min, and the sensor output (EMF) showed continuously reversible response. The measured EMF variation with the CO_2 concentration is plotted as a function of the logarithm of the CO_2 partial pressure in Figure 4.3 with the theoretical slope (solid line) calculated from the equation (4-7). The sensor output obtained by changing the CO_2 concentration lies in a linear relationship, and the n value obtained from the measured EMF slope is 1.97 which almost obeys the Nernst equation (4-7) (n=2.00).

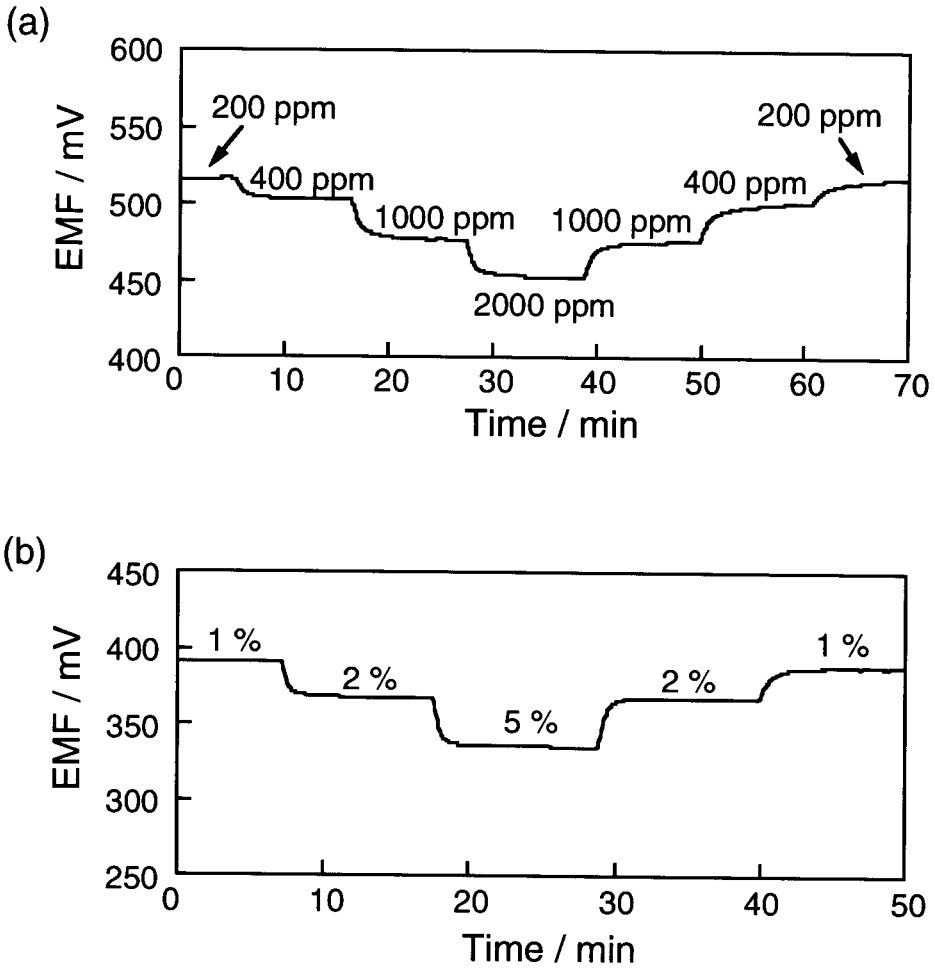

Figure 4.2. One of representative sensor response curves of the present CO_2 sensor at 550 ˚C((a) 200 – 2000 ppm, (b) 1 – 5 %) in dry atmosphere.

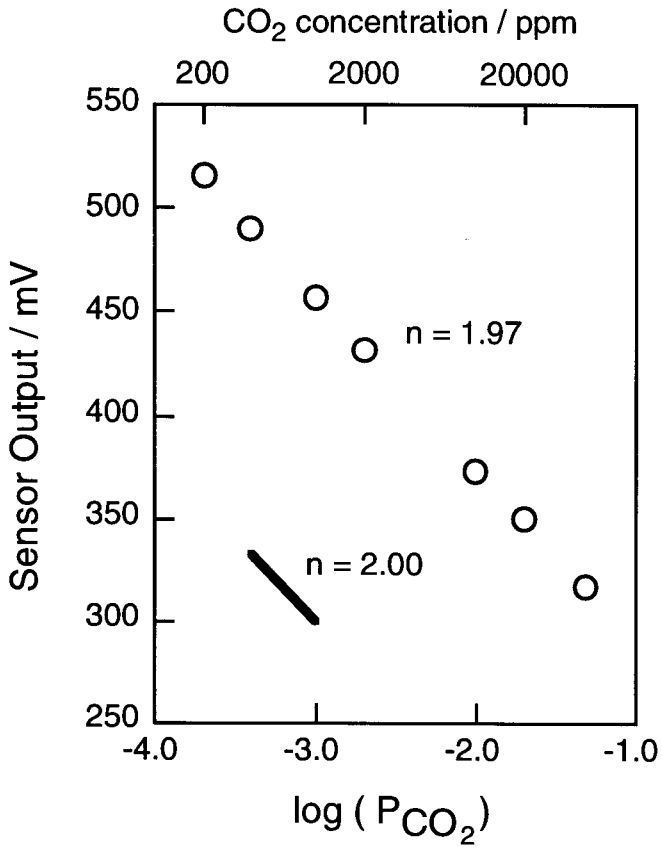

Figure 4.3. The relation between the sensor output and the logarithm of the CO_2 concentration at 550 °C in dry atmosphere.

Since the other gas species such as nitrogen oxides (NOx) and H_2O coexist and the oxygen concentration continuously changes in an emitted gas atmosphere, a highly selective CO_2 sensing is required for practical sensors. The effect of the coexistence of NOx, O_2 and H_2O on the CO_2 sensing was investigated over 12h with changing gases concentration. The EMFs of the present sensor at 1% CO_2 with O_2 from 5 to 40 vol% and with NOx from 0 to 500 ppm are depicted in Figures 4.4 and 4.5, respectively. As expected from the proposed reaction mechanism (eq. (4.6)), no interference with the coexistence of O_2 was observed. Furthermore, NOx which always appears in an exhaust gas to a certain content was also found not to interfere with the CO_2 sensing at all.

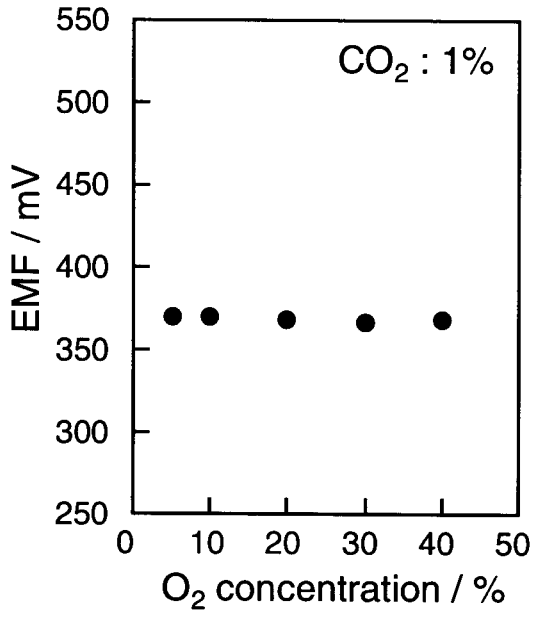

Figure 4.4. The sensor output variation in the atmosphere of 1% CO_2 with O_2(5 to 40 vol%) at 550 ˚C.

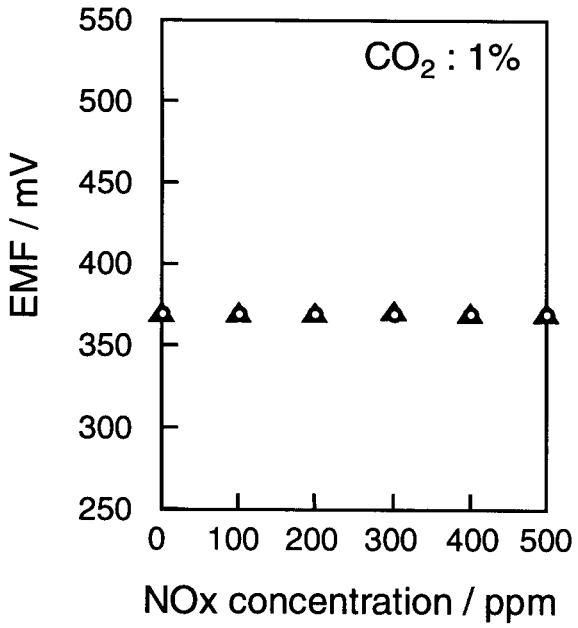

Figure 4.5. The EMF variation in the atmosphere of 1% CO_2 with the coexistence of NOx(0 – 500 ppm) at 550 ˚C (▲ : NO, ○ : NO_2).

The EMF variation with the CO_2 concentration coexisted with H_2O is plotted as a function of the logarithm of the CO_2 partial pressure in Figure 4.6. No meaningful difference of EMF in between dry and wet atmospheres (even in the atmosphere where the water vapor exists up to 30 vol%) was observed. The above mentioned results explicitly indicate that the sensor can be applied in various types of exhaust gas atmosphere.

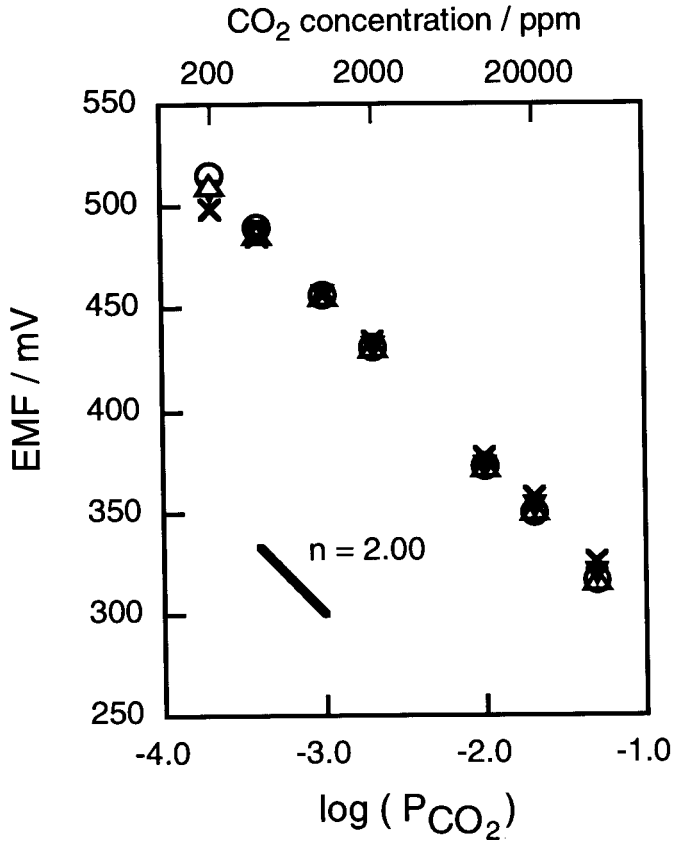

Figure 4.6. The relationship between the EMF and the logarithm of the CO_2 concentration at 550 °C in wet air where water vapor exists 4.2 vol% (△), 10 vol% (▲), 30 vol% (×). The data for the relation in dry air (○) is also plotted.

For the purpose of applying the present sensor in an actual detecting site, a long–term stability of the sensor output is greatly requested. Figure 4.7 shows the sensor output deviation of the $Sc_{1/3}Zr_2(PO_4)_3$ based sensor at the CO_2 content of 400 ppm and 2000 ppm. In the case of a sensor fabricated with a Li^+ ion conductor with YSZ, the EMF shifts [55] as shown in Figure 7 as

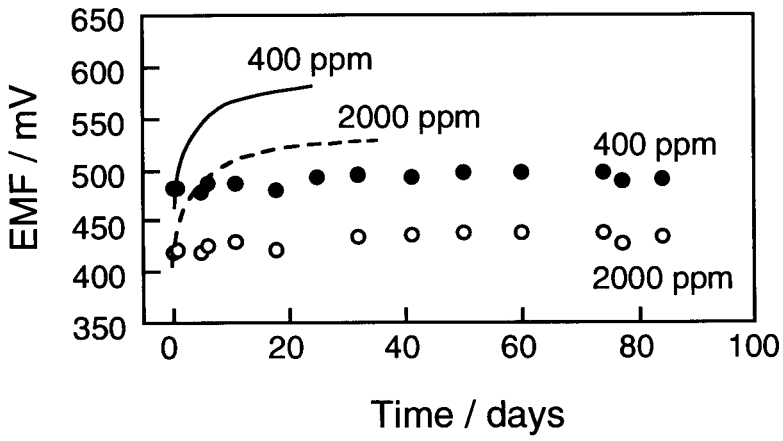

Figure 4.7. The EMF variation with the day span of the $Sc_{1/3}Zr_2(PO_4)_3$ based sensor at the CO_2 concentration of 400 ppm(●) and 2000 ppm(○). The corresponding data for the sensor with Li^+ conductor are also shown as solid (400 ppm) and broken line (2000 ppm).

solid (400 ppm) and broken lines (2000 ppm), especially after a week from the operation because the EMF strongly depends on the activity of the oxide, Li_2O, and its activity easily changes at first stage. After 10 days from the operation, the EMF variation reached c.a. 100 mV. In contrast, the EMF outputs at 400 and 2000 ppm for the sensor based on $Sc_{1/3}Zr_2(PO_4)_3$ does not show any meaningful EMF deviation from the operation. Both a high initial stability and also a long–term stability are realized owing to the stability of the compound formed at the interface between trivalent Sc^{3+} ion conducting solid electrolyte and YSZ, that is, Sc_2O_3.

4.4. Conclusions

The compact sensor based on $Sc_{1/3}Zr_2(PO_4)_3$ and YSZ solid electrolytes with Li_2CO_3 as the auxiliary electrode was found to show not only a high sensitivity but also a high selectivity for CO_2 sensing with a rapid (the time necessary for 90% response is within 1 min) and reproducible response. Because $Sc_{1/3}Zr_2(PO_4)_3$ has both a high chemical stability and a high mechanical strength, the present sensor was found to operate in various atmosphere changing from clean to dirty and dry to wet, and is expected to be a promising sensing tool applicable for various fields.

Summary

In this work of this thesis, the demonstration of trivalent cation conduction in solid, development of novel trivalent cationic conductors with a high chemical and a high physical stability, and the application of trivalent cation conducting solid electrolyte, were described. The results obtained through this work are summarized as follows:

Chapter 1.

In order to estimate the trivalent cation conduction in $Sc_2(WO_4)_3$ type structure, the potential energies around Al and W in $Al_2(WO_4)_3$ single crystal, calculation of the electrostatic forces between migrating trivalent cation and surrounding ions in $Sc_2(WO_4)_3$ structure, and the diffusion coefficient of trivalent cation were investigated. All data support strongly the trivalent cation conduction in $Sc_2(WO_4)_3$ type solid electrolytes, and the significance of inclusion of high valence cation than trivalent for the trivalent cation conduction is also revealed. Furthermore, anisotropic conducting behavior in the $Sc_2(WO_4)_3$ type structure was explained from the results of the calculation for the electrostatic forces in each conducting plane.

Chapter 2.

The $R_{1/3}Zr_2(PO_4)_3$ with NASICON–type structure was newly developed by a sol–gel method in order to improve the demerits of the $Sc_2(WO_4)_3$ type tungstates. The suitable lattice size for trivalent R^{3+} ion conduction in $R_{1/3}Zr_2(PO_4)_3$ with NASICON type structure was obtained for $Sc_{1/3}Zr_2(PO_4)_3$ which is composed of the smallest trivalent cation of Sc^{3+} among the rare earth series. With decreasing the R^{3+} size in the $R_{1/3}Zr_2(PO_4)_3$, the trivalent ion conductivity monotonously increased, and the $Sc_{1/3}Zr_2(PO_4)_3$ shows the highest conductivity which is comparable value of that for the $Sc_2(WO_4)_3$ type solid electrolyte series.

Chapter 3.

The $R_{1/3}Zr_2(PO_4)_3$ with NASICON type structure was prepared by a ball milling method as a new sinthesizing method in order to enhance the crystallinity of the sample. The conductivity of the $R_{1/3}Zr_2(PO_4)_3$ was increased about 3 times in comparison with that of the sample prepared by the sol–gel method, and the conductivity for the $Sc_{1/3}Zr_2(PO_4)_3$ reached the value of $Sc_2(WO_4)_3$, which is the highest trivalent cation conductivity in the tungstate series. The enhancement of the conductivity and reduction of the activation energy was resulted from the formation of the conducting pathway by through the metastable phase of amorphous state, and from the increase of the sample crystallinity and ordering the ion in the lattice.

Chapter 4.

The compact sensor based on $Sc_{1/3}Zr_2(PO_4)_3$ and YSZ solid electrolytes with Li_2CO_3 as the auxiliary electrode was found to show not only a high sensitivity but also a high selectivity for CO_2 sensing with a rapid (the time necessary for 90% response is within 1 min) and reproducible response. Because $Sc_{1/3}Zr_2(PO_4)_3$ has both a high chemical stability and a high mechanical strength, the present sensor was found to operate in various atmosphere changing from clean to dirty and dry to wet, and is expected to be a promising sensing tool applicable for various fields.

References

[1] T. Kudo, K. Fueki, *Solid State Ionics*, Kodansha, Tokyo, 1990.

[2] A. R. West, *Solid State Chemistry and its Applications*, John Wiley & Sons, Chichester, (1984), p. 453.

[3] S. Ikeda, M. Takahashi, J. Ishikawa, and K. Ito, *Solid State Ionics*, **23**, 125 (1987).

[4] K. Nomura, S. Ikeda, K. Ito, and H. Einaga, *Bull. Chem. Soc. Jpn.*, **65**, 3221 (1992).

[5] K. Nomura, S. Ikeda, K. Ito, and H. Einaga, .*Chem. Lett.*, **1992**, 1897.

[6] K. Nomura, S. Ikeda, K. Ito, and H. Einaga, *Solid State Ionics*, **61**, 293 (1993).

[7] N. Imanaka, Y. Okazaki, and G. Adachi, *J. Mater. Chem.*, **10**, 1431 (2000).

[8] G. Dorner, H. Durakpasa, G. Fafilek, and M. W. Breiter, *Solid State Ionics*, **53–56**, 553 (1992).

[9] K. W. Semkow and A. F. Sammells, *J. Electrochem. Soc.*, **135**, 244 (1988).

[10] G. C. Farrington and B. Dunn, Solid State Ionics, 7, 267 (1982).

[11] R. Seevers, J. DeNuzzio, G. C. Farrington and B. Dunn, *J. Solid State Chem.*, **50**, 146 (1983).

[12] J. B. Goodenough, H. Y–P. Hong, and J. A. Kafaras, *Mater. Res. Bull.*, **11**, 203 (1976).

[13] P. G. Bruce and I. Abrahams, *J. Solid State Chem.*, **95**, 74 (1991).

[14] B. Dunn and G. C. farrington, *Solid State Ionics*, **9&10**, 223 (1983).

[15] W. Carrillo–Cabrera, J. O. Thomas, and G. C. Farrington, *Solid State Ionics*, **9&10**, 245 (1983).

[16] B. Ghosal, E. A. Mangle, M. R. Topp, B. Dunn, and G. C. Farrington, *Solid State Ionics*, **9&10**, 273 (1983).

[17] G. C. Farrington, B. Dunn, and J. O. Thomas, *Appl. Phys.*, **A32**, 159 (1983).

[18] T. Dedecke, J. Köhler, F. Tietz, and W. Urland, Eur. *J. Solid State Inorg. Chem.*, **33**, 185 (1996)

[19] J. Köhler and W. Urland, *Solid State Ionics*, **86–88**, 93 (1996).

[20] J. Köhler, G. Balzer–Jöllenbeck, and W. Urland, *J. Solid State chem..*, **122**, 315 (1996).

[21] J. Köhler and W. Urland, *Angew. Chem.*, **109**, 105 (1997).

[22] A. M. George and A. N. Virkar, *J. Phys. Chem. Solids*, **49**, 743 (1988).

[23] T. E. Warner, D. J. Fray, and A. Davies, *Solid State Ionics*, **92**, 99 (1996).

[24] T. E. Warner, D. J. Fray, and A. Davies, *J. Mater. Sci.*, **32**, 279 (1997).

[25] Y. Kobayashi, T. Egawa, S. Tamura, N. Imanaka, and G. Adachi, *Chem. Mater.*, **9**, 1649 (1997).

[26] N. Imanaka, Y. Kobayashi, S. Tamura, and G. Adachi, *Electrochem. and Solid-State Letters*, **1**, 271 (1998).

[27] Y. Kobayashi, T. Egawa, Y. Okazaki, S. Tamura, N. Imanaka, and G. Adachi, *Solid State Ionics*, **111**, 59 (1998).

[28] N. Imanaka, Y. Kobayashi, K. Fujiwara, T. Asano, Y. Okazaki, and G. Adachi, *Chem. Mater.*, **10**, 2006 (1998).

[29] J. Köhler, N. Imanaka, and G. Adachi, *Chem. Mater.*, **10**, 3790 (1998).

[30] N. Imanaka and G. Adachi, *Molten Salts*, **41**, 177 (1998).

[31] Y. Kobayashi, S. Tamura, N. Imanaka, and G. Adachi, *Solid State Ionics*, **113-115**, 545 (1998).

[32] J. Köhler, Y. Kobayashi, N. Imanaka and G. Adachi, *Solid State Ionics*, **113-115**, 553 (1998).

[33] Y. Kobayashi, T. Egawa, S. Tamura, N. Imanaka, and G. Adachi, *Solid State Ionics*, **118**, 325 (1999).

[34] J. Köhler, N. Imanaka and G. Adachi, *Solid State Ionics*, **122**, 173 (1999).

[35] N. Imanaka, Y. Okazaki, Y. Kobayashi, S. Tamura, T. Asano, T. Egawa, and G. Adachi, *Solid State Ionics*, **126**, 41 (1999).

[36] N. Imanaka, Y. Okazaki, and G. Adachi, *J. Mater. Chem.*, **10**, 1431 (2000).

[37] N. Imanaka, T. Ueda, Y. Okazaki, S. Tamura, and G. Adachi, *Chem. Mater.*, **12**, 1910 (2000).

[38] H. Adachi, M. Tsukada, C. Satoko, *J. Phys. Soc. Japan*, **45**, 875 (1978).

[39] N. Imanaka, S. Tamura, M. Hiraiwa, G. Adachi, H. Dabkowska, A. Dabkowski, and J. E. Greedan, *Chem. Mater*, **10**, 2542 (1998).

[40] M. Hiraiwa, S. Tamura, N. Imanaka, G. Adachi, H. Dabkowska and A. Dabkowski, *Solid Sate Ionics*, **136–137**, 427 (2000).

[41] B. Dawson and B. T. M. Willis, *Proc. R. Soc. London Ser A*, **298**, 307 (1967).

[42] B. T. M. Willis, *Acta Cryst.*, ,**A 25**, 277 (1969).

[43] K. Tanaka and F. Marumo, *Acta Cryst.*, **A 39**, 631 (1983).

[44] M. A. Talbi, R. Brochu, C. Parent, L. Rabardel, and G. L. Flem, *J. Solid State Chem.*, **110**, 350 (1994).

[45] H. Aono, N. Imanaka, and G. Adachi, *Accounts of Chemical Research*, **27**, 265 (1994).

[46] A. Haeusler and J-U. Mayer, *Sensors and Actuators*, **B 34** , 388 (1996).

[47] T. Ishihara, K. Kometani, Y. Mizuhara, and Y. Takita, *Sensors and Actuators*, **B 5**, 97 (1991).

[48] J. Tamaki, M. Akiyama, C. Xu, N. Yamazoe, and N. Miura, *Chem.Lett.*, **1990**, 1243–1246.

[49] S. Yao, S. Hosohara, Y. Shimizu, N. Miura, H. Futata, and N. Yamazoe, *Chem. Lett.*, **1991**, 2069–2072.

[50] S. Ikeda, S. Kato, K. Nomura, K. Ito, H. Einaga, S. Saito, and Y. Fujita, *Solid State Ionics*, **70/71**, 569 (1994).

[51] N. Miura, S. Yao, S. Nonaka, and N. Yamazoe, *J. Mater. Chem.*, **5**, 1391 (1995).

[52] N. Imanaka, T. Murata, and G. Adachi, *Denki-kagaku oyobi Kogyo Buturi Kagaku*, **61**, 909 (1993).

[53] N. Imanaka, Y. Hirota, and G. Adachi, *Sens. Actuators*, **B 25**, 380 (1995).

[54] N. Imanaka, M. Kamikawa, S. Tamura, and G. Adachi, *Electrochem. Solid-State Lett.*, **2**,

602 (1999).

[55] N. Imanaka, T. Yamamoto, G. Adachi, *Chem.Lett.* **1990**, 1243.

Acknowledgment

The author would like to express his heartfelt gratitude to Professor Dr. Gin-ya Adachi, Department of Applied chemistry, Faculty of Engineering, Osaka University, for his continuous guidance, his invaluable suggestions, and his science encouragement throughout the work. The author is indebted to Dr. Nobuhito Imanaka for his continuous guidance and stimulating discussions for carrying out this work.

The author would also like to thank Professor Dr. Ken-ichi Machida, Collaborative Research Center for Advanced Science and Technology, Osaka University, for his valuable comments and suggestions.

The author is also very grateful to Dr. Hiroki Sakaguchi, Department of Materials Science, Faculty of Engineering, Tottori University, and Dr. Toshiyuki Masui, Department of Applied Chemistry, Faculty of Engineering, Osaka University, for their helpful suggestions and heartfelt advice. Furthermore, the author is obliged to Professor Dr. Kiyoaki Tanaka, Department of Materials Science & Engineering, Faculty of Engineering, Nagoya Institute & Technology, for potential energy analysis, Dr. K Yamada, Hyogo Prefectural Institute of Technology, for EPMA and SEM measurements.

Special thanks should be given to author's co-workers, Dr. Yasuyuki Kobayashi, Mr. Takuya Asano, Mr. Takashi Egawa, Mr. Takao Yamamoto, Ms. Sen-ri Yoshikawa, Mr. Yusuke Okazaki, Mr. Masamichi Hiraiwa, Mr. Tomohiro Ueda, Mr. Masayuki Kamikawa, Mr. Koji Okamoto, Mr. Masaharu Itaya, Mr. Akio Ogura, Ms. Misato Yamaguchi, Dr. Ken-ji Toda, and Dr. Joachim Köhler for their helpful assistance and support in the course of this work, and members of the research group under direction of Professor Dr. G. Adachi, Osaka University. The Japan Society for the Promotion of Science is also acknowledged for a research fellowship.

Finally, the author is particularly grateful to his parents, Mr. Shin-ichi Tamura and Mrs. Miyoko Tamura, his brothers, Mr. Katsuhiro Tamura, Mr. Mitsuo Tamura, and his fiancee, Ms.

Keiko Kishimoto, who have been understanding and supporting him.